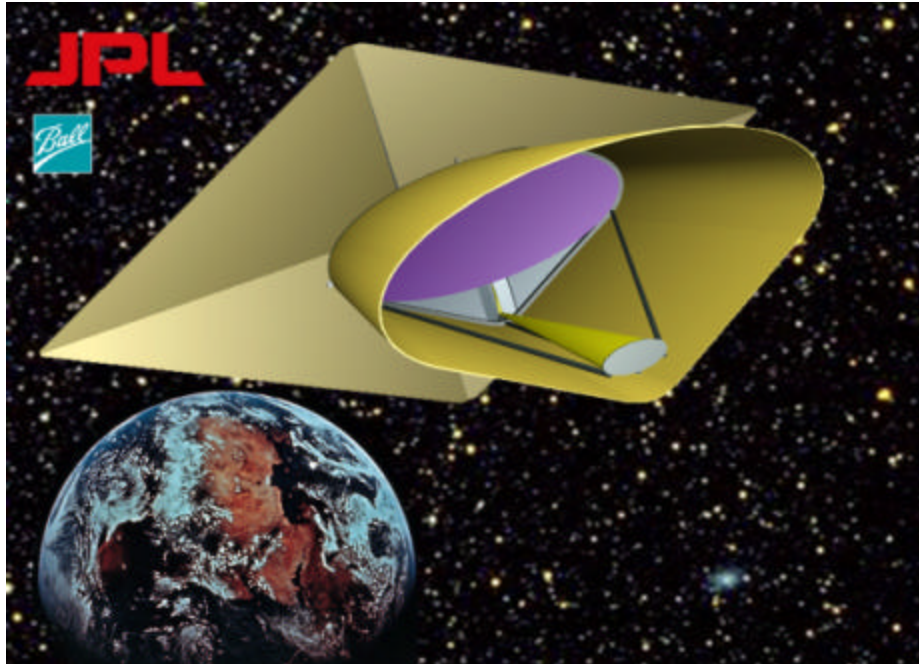


Terrestrial Planet Finder Architecture Study

Final Report -- March 29, 2002

Ball Aerospace & Technologies Corp.



The Ball Aerospace TPF Team		Science Team		Engineering Team	
		Member	Institution	Member	Institution
Ball Management Team		Ron Allen	STScI	Jim Austin	Ball
Member	Role	John Bally	U. of Colorado/CASA	Jeff Bladt	Ball
Jerry Chodil	VP, Civil Space Sys.	Peter Bender	U. of Colorado/JILA	Ira Becker	Ball
Jim Crocker	NGST Prog. Mgr.	Torsten Böker	STScI	Wayne Davis	Ball
Hugh Davis	Deputy Prog. Mgr.	Alan Boss	Carnegie Inst. Wash.	Billy Derbes	L'Garde
Dave Fischer	Deputy Prog. Mgr.	Robert Brown	STScI- Prin. Scientist	Edgar Choueiri	Princeton
Steve Kilston	Program Manager	Tim Brown	UCAR/HAO	Porter Davis	Honeywell
Vera Kilston	Presentations	Chris Burrows	Consultant	William Deinger	Ball
Terry Lapotosky	ITAR Regulations	Webster Cash	U. of Colorado/CASA	Gene Dryden	Aerojet
Beth McGilvray	ITAR Compliance	Dennis Ebbets	Ball	Kenny Epstein	Ball- Pr.Eng.
Janet Phillips	TAA's	Christ Ftaclas	U. of Hawaii	Joe Girard	Ball
Harold Reitsema	Executive Liaison	Norm Jarosik	Princeton	Carl Gelderloos	Ball
Doak Woodruff	Contracts	Jeremy Kasdin	Princeton	Pini Gurfil	Princeton
Lisa Yedo	Finance	Jim Kasting	Penn State	Paul Hannan	Ball
		Marc Kuchner	Ctr. for Astrophysics	Tim Hawarden	Edinburgh
		Steve Lubow	STScI	Tupper Hyde	Honeywell
		D. Mozurkewich	Naval Research Labs	John Lesveaux	Kodak
		Jerry Nelson	UCSC	Mike Lieber	Ball
		Charley Noecker	Ball	Mike Littman	Princeton
		Alan Penny	Rutherford-Appleton	Jim Lundahl	Ball
		A. Quirrenbach	UCSD	Richard Miles	Princeton
		Sara Seager	Carnegie Inst. Wash.	Dan Peters	Ball
		David Spergel	Princeton	Dan Quenon	Honeywell
		Robin Stebbins	NASA Goddard	Pete Thomas	Consultant
		Charlie Telesco	U. of Florida	Francis Thompson	Aerojet
		Wes Traub	Ctr. for Astrophysics	Rebecca Walter	Ball
		Ed Turner	Princeton	Doug Wiemer	Ball
		Bob Woodruff	Ball	Jeff Wynn	Kodak

Ball Aerospace TPF Architecture Study Part 1 -- Preliminary Architecture Study

1 Approach

1.1 Philosophy -- Joining Potential Concepts to TPF Mission Criteria

Throughout our TPF Preliminary Architecture Review, the Ball team strove to be open-minded about any design concept with significant potential to detect extra-solar terrestrial planets. Towards this end, a team of very experienced yet wide-ranging members was assembled. From the beginning we asked them for all their relevant ideas, and conducted energetic and enthusiastic brainstorming sessions which stimulated invention of entirely original concepts (the bottom-up direction). With 30 different approaches suggested, a proponent was assigned to lead each one's investigation, and to bring to our joint discussions benefits and problems identified for that approach. These spirited meetings allowed sharing many different viewpoints and experience bases covering science and technology possibilities and limitations, resulting in the elucidation of many design features which were combined later into the Ball team's final design descriptions. Contributions came both from scientists (photon sources) and technologists (photon detectors), ensuring from the start a balanced approach between dream and reality. This process is shown in Figure 1.1-1

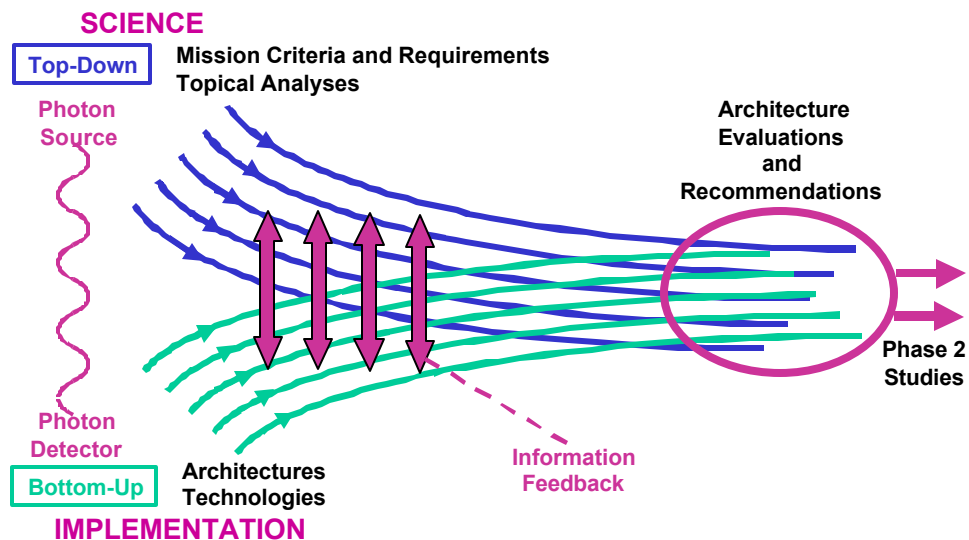


Figure 1.1-1 Our Combined Top-Down and Bottom-Up Approach

Our initial efforts also focused on studying and understanding the requirements for effective planet identification and characterization (the top-down direction). This included an extensive study of phenomenologies expected for target planet and star properties, the detectability of biomarkers, and the properties of astrophysical objects of interest. Just as for our own planet, an extrasolar terrestrial planet would have two peaks in its spectrum: the peak nearly identical to that in the stellar spectrum the planet reflects, and the peak due to thermal emission from the planet itself. It then became apparent that in our brainstorming efforts we were dealing with two main families of design concepts: those aiming to detect the reflected light (at visible wavelengths) and those aiming to detect the emitted light (at mid-infrared wavelengths). Therefore, we divided our research similarly, for efficiency, into thinking about two main larger groups, each with many similar properties for each group member. (Miscellaneous planet-finding concepts not capable of directly collecting planet light were called "diversity" architectures, which we described but did not analyze.) We also accounted for promising capabilities to perform astrophysical observations which might eventually be achievable with each concept. This study organization is summarized in Figure 1.1-2.

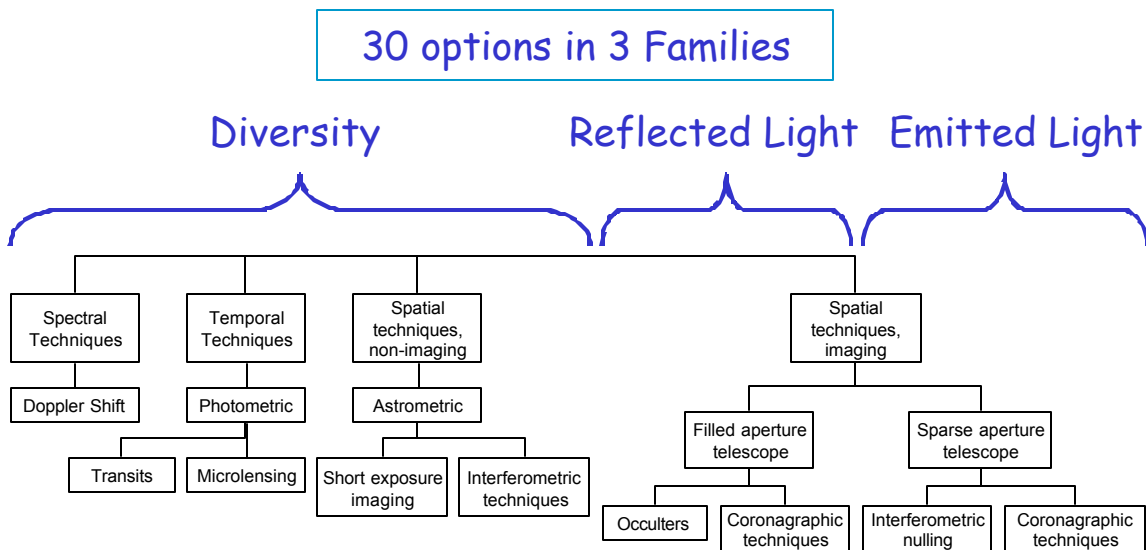


Figure 1.1-2 Candidate Architecture Families Considered

1.2 Requirements Development

Our next step was to derive, from the basic mission requirements, the driving science and technological requirements for each candidate architecture, to help refine each concept, and eventually to enable an initial comparison and later evaluation. This was done by examining Request for Proposal (RFP) and Science Working Group inputs and analyzing the candidate designs according to the seven criteria the RFP set forth. These are shown in Figure 1.2-1 below.

- #1: Sensitivity in finding and characterizing exoplanets
- #2: Richness of astrophysical science opportunities
- #3: Technology development needed
- #4: Life cycle costs
- #5: Risk of cost, technology, schedule, on-orbit failures
- #6: Reliability and robustness
- #7: Alignment with the technology path to future exoplanet-study missions

Figure 1.2-1 The Seven Evaluation Criteria for TFP Architectures

For each of these areas we identified the key issues affecting satisfaction of requirements and constraints, and began to optimize the designs. The driving performance factors were:

- Angular resolution
- Minimum angular star-planet separation (Inner Working Distance, IWD) at which light from the central star could be suppressed sufficiently to allow detection of an Earth-like planet
- Reduction of starlight leakage into the detectors measuring the planet signal
- Signal-to-noise ratio (SNR) and integration time
- Atmospheric spectra and biomarkers
- Wavelength bands

Usable fields of view
Implications of the true star sample for the number of systems that could be investigated
Impact of noise and confusion from other astronomical sources
Astrophysics performance

The quantitative levels for the main science requirements were provided in a Design Reference Program (DRP) by the TPF Science Working Group (SWG). The most significant science requirement was that “TPF must detect radiation from any Earth-like planets in the habitable zones surrounding ~150 solar type (spectral types F, G, and K) stars. TPF must: 1) characterize the orbital and physical properties of all detected planets to assess their habitability; and 2) characterize the atmospheres and search for potential biomarkers among the brightest candidates for Earth-like planets.”

We began to flow down these requirements to the performance factors under the following assumptions:

Detect — Repeatable observations with SNR of at least 5
Earth-like Planets — Planets with one-half to twice the radius of Earth
Habitable Zone (HZ) — The locus of orbits where an Earth-sized planet would be heated by its star to temperatures permitting liquid H₂O retention at 1 atm pressure (which could involve some planet and atmosphere evolution)
150 FGK Stars — Nearby representatives of these stellar types luminous enough and close enough to us for any Earth-like planets in their habitable zones to be viewable at angular separations from their stars large enough to be detected, and with apparent brightnesses enabling detections of the planets and selected spectral features within integration times permitting TPF mission completion.

1.3 *Identifying the Critical Issues*

In evaluating our many concepts, we decided that, for exoplanets, “better” science performance means:

More stars surveyed, more planets found, and more planets characterized
Planets better characterized (i.e., more information gathered that is helpful with interpretations).

This led us to find a “key tradeoff” between:

- (1) Required integration time, and
- (2) Inner working distance (IWD) capability.

To get relevant answers for this key tradeoff, we performed a detailed analysis of the true star sample. Our approach to this analysis involved the following steps:

Extracted sample population from Hipparcos main catalog, using parallax and B-V color
Limited candidates to single, non-variable, main-sequence stars
Inferred stellar parameters from textbook relationships
Constructed H-R diagram
Derived HZ from Kasting planetary model atmospheres and correlation with stellar parameters
Computed angular separations for inner, mid, and outer limits of HZ
Estimated planet brightness in reflected light (V band)
Estimated planet brightness in emitted thermal radiation (N band)
Examined distributions, correlations, trends

A main result of the star sample analysis was the need for a system performing the full TPF mission to be able to reach a small IWD, approximately 40 milliarcseconds (mas). This is evident in Figure 1.3-1.

An additional factor in needing a small IWD is the expectation that planetary system orbital planes will probably be distributed at random inclinations to the plane of the sky, with the consequence that more systems will appear close to edge-on than face-on. Therefore, during many of our attempts to view a planet, it will be undetectable because it is nearly in front of or behind its star, appearing at much smaller

angular separation than at maximum elongation. Some quantitative analysis showed that this factor is not a huge concern, however: 70% of the time the angular separation will, on the average, still exceed 70% of that at maximum elongation. However, it does make it desirable to have the capability of achieving an IWD of 35 mas to ensure that for the full sample of 150 stars we can see detected planets often enough to characterize their orbits fairly well.

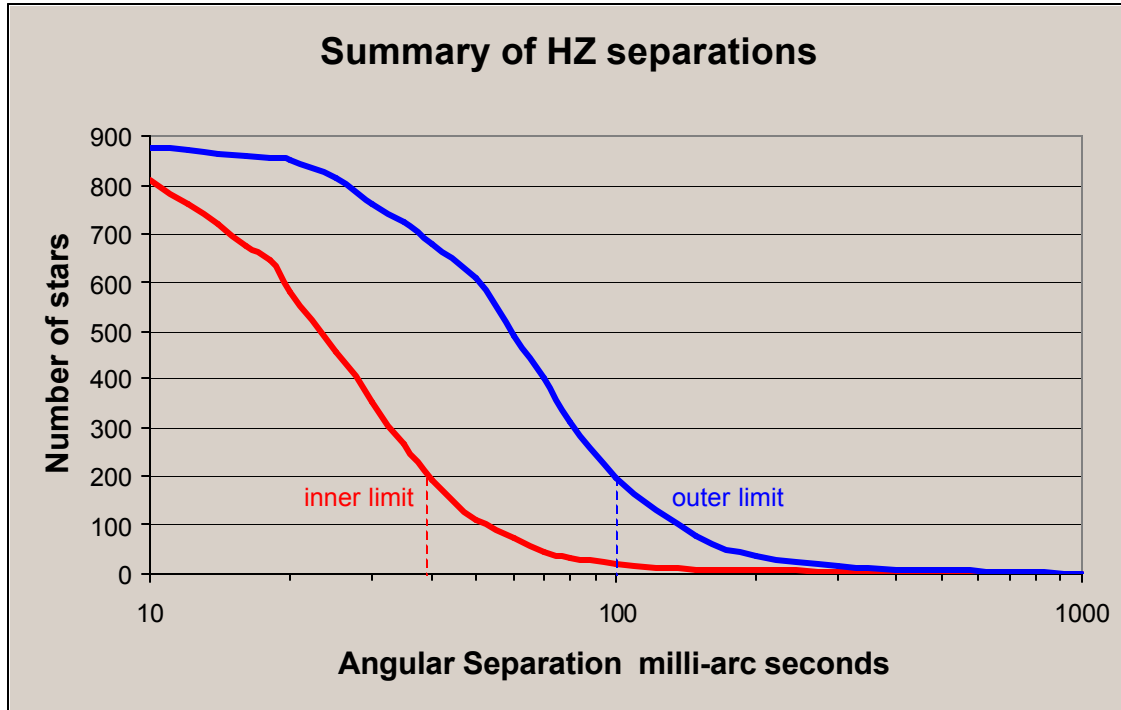


Figure 1.3-1 Number of Candidate Stars Habitable Zones Fully Searchable vs. IWD (red)

We identified the biomarkers which we think measure habitability (our work is included in the Biomarker Report Summary earlier in this volume); these included:

- Atmospheric chemical constituents (at both visible and MIR wavelengths, several are detectable)
- Planet temperature (from IR continuum, orbital radius, star luminosity), and
- Secular variations (indicating rotation period or actual seasonal changes).

Since it affects our evaluation of a terrestrial planet’s history and habitability, we also recognized the value of achieving a broader understanding of all the properties of a planetary system’s constituents, e.g., both gas giant and terrestrial planets, and debris disks. Therefore the ability to search near a star from ~ 0.5 AU out to ~ 20 AU and detect any major planets present was also seen as a strong advantage of any concept.

In evaluating our variety of concepts, we of course also accounted for many technology factors, such as the size and number of collectors, thermal and vibrational stability, robustness, ease of launch, and operational reliability. In addition, we also considered the programmatic factors such as risk, cost, and schedule, as well as the applicability of the candidate designs to downstream Origins programs.

2 Concepts Investigated

We examined in detail the characteristics of both the reflected-light and emitted-light families and then described the most promising candidates within each family.

2.1 Reflected-Light Options

The relative insensitivity of this architecture family to exozodiacal light and background clutter in visible wavelengths eliminates a large source of potential performance degradation. The use of a detector array in coronagraph designs leads to some pixels receiving a fairly uncontaminated and informative signal from the planet, potentially revealing - with a single observation - the existence of terrestrial and other planets near a star. Little residual starlight or local or exozodi light will hit the planet pixels. Planet discoveries should be more rapid with a direct viewing technique than with the extensive repositioning an interferometer requires. The visible spectrum contains significant biomarkers and possibly could even permit detection of chlorophyll, a most significant life indicator. Also, planned follow-on missions to TPF, such as Planet Imager, will very likely require large-aperture visible coronagraph components, as well as long-baseline interferometric techniques.

Because of the very high ratio of total stellar to total planet flux at visible wavelengths, perhaps the most challenging technological hurdle for a TPF coronagraph is the size and optical quality of the primary mirror required to suppress starlight in order to see a planet at angles very close to its star. A very large aperture is needed to collect the modest number of planet photons and also to provide high resolution of the closely spaced objects, thus ensuring sufficient planet contrast against the residual starlight. Without nearly perfect wavefront quality and scatter control, stray starlight would mix with the light from the planet and contaminate the signal. We have developed detailed models for the magnitude of the scattered light as a function of the size of the optical defects, as well as algorithms for correcting the wavefront using a deformable mirror based on data collected from the science detector array (not requiring any separate wavefront sensing components). The basic layout for a coronagraph is shown in Figure 2.1-1.

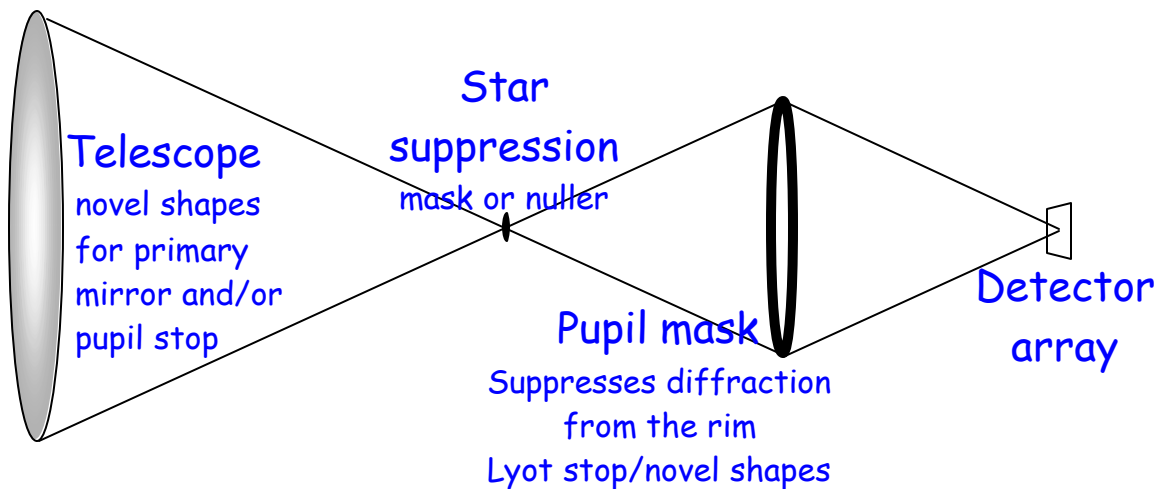


Figure 2.1-1 Basic Coronagraph Features

A large-aperture telescope, potentially with an elliptical entrance aperture (to fit inside existing or expected launcher fairings), concentrates the starlight at a very small spot in an image plane. At that position, coronagraphic suppression of the starlight can be via a mask or a nuller (using destructive interference). The instrument can also or alternatively employ one or more pupil masks (a pupil is the location of an image of the entrance aperture formed by the optical train) to direct the starlight away from parts of the

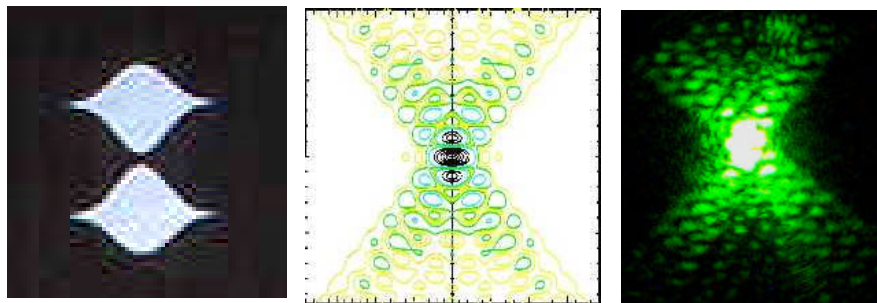
image plane where a planet is to be detected. The actual optical design would almost certainly be off-axis, to better control diffracted starlight, and have a Deformable Mirror (DM) for wavefront control.

The following are the reflected-light options that seemed to have greatest merit. For practical use in the TPF missions, nearly all these coronagraphs should provide sensitivity at wavelengths from about 0.3 to 2 μ m, be capable of spectral resolutions from 1 to 100, and require entrance apertures of about 30 m^2 . They would be placed in an L2 or heliocentric drift-away orbit, and be capable of sky coverage anywhere more than 60 degrees away from the sun direction. They would be able to detect Earth-like planets with angular separations from their host stars of at least 40 mas, and could provide angular resolutions on the order of 10 mas for imaging exoplanetary systems and objects of astrophysical interest. Their optical configurations in most cases permit incorporation of other instruments using the same primary mirror, by means of field sharing or via use of a flip mirror. Such instruments could include wide-field imagers and spectrographs.

2.1.1 Spergel Variable Pupil Coronagraph

A very creative analysis by David Spergel resulted in the design of an optimum shape for the telescope aperture (or interior pupil stop) which would change the spatial distribution of starlight (focused on the detector array) from the standard Airy pattern to a diffraction pattern which falls off very quickly with field angle in two opposite sectors of the image plane. In those two sectors, planets can then be detected at small angles from their stars, but field rotation is needed to search an entire planetary system.

The shape of the Spergel (later developed into the Spergel/Kasdin) pupil [Spergel 2000, Kasdin, Spergel, and Littman 2002], and both an expected theoretical and an actual resultant image pattern (point-spread function, PSF, with monochromatic laser light) are shown in Figure 2.1-2 below. Most of the starlight suppression is accomplished with the shaped pupil alone, but an image plane mask can also be added to prevent the large amount of starlight at that position from getting farther into the optical system, bouncing around and then landing on the detector array.



Spergel pupil PSF (theor.) 1st Lab Demo

Figure 2.1-2 The Spergel Pupil

2.1.2 Masking Coronagraph

The classical (masking) coronagraph is currently better understood than shaped-pupil options, because it has been used and studied much longer. For example, we know that the image-plane mask can have a transmission varying radially as one minus a gaussian function of the radial distance from the position of the stellar image. We are also studying other mask designs [e.g., Kuchner and Traub, 2002], potentially offering higher performance. An image-plane mask tends to keep most of the starlight out of the central part of the focal plane's stellar image position, but also scatters some starlight toward outer regions in the pupil plane, downstream from the mask. Therefore a ring-shaped Lyot stop is used at that pupil to further diminish the starlight at the focal plane. Figure 2.1-3 shows the basic optical layout.

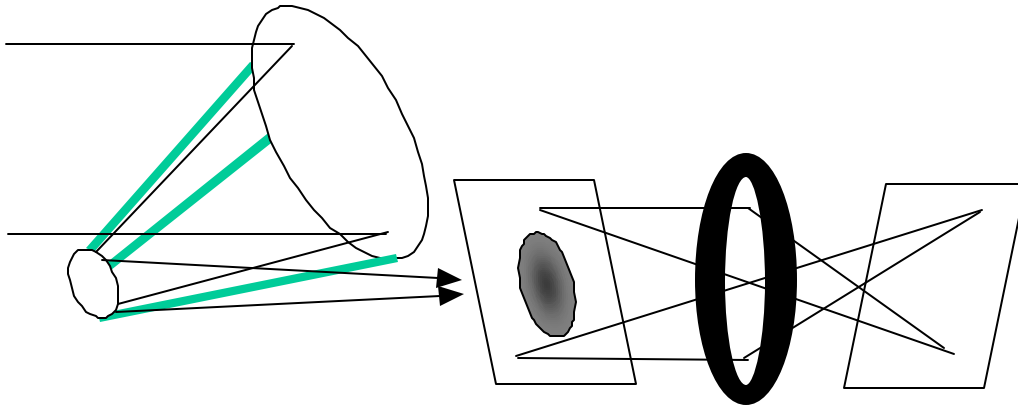


Figure 2.1-3 The Mask and Lyot stop of the Masking Coronagraph

With a masking coronagraph it's possible to view the entire circumstellar region at once, or at least one half of it (for particular ways of using the DM to correct for system transmission non-uniformities). That reduces the number of telescope orientations needed, and thus the search time, to find extrasolar planets.

2.1.3 Nulling Coronagraph

The nulling coronagraph uses interferometric elements (perhaps a cats-eye or a rotation-shearing nuller) to produce destructive interference (nulling) of the recombined starlight after it has been split into two optical paths, while permitting constructive interference for off-axis sources such as the target extrasolar planets. Obviously, highly accurate pathlength control is needed, and inherent image doubling complicates image interpretation. However, the nulling coronagraph does offer the potential of detecting planets within the first few Airy rings, and thus very close to their host stars. Figure 2.1-4 shows the layout of a nulling coronagraph, depicting the double image expected for any object viewed.

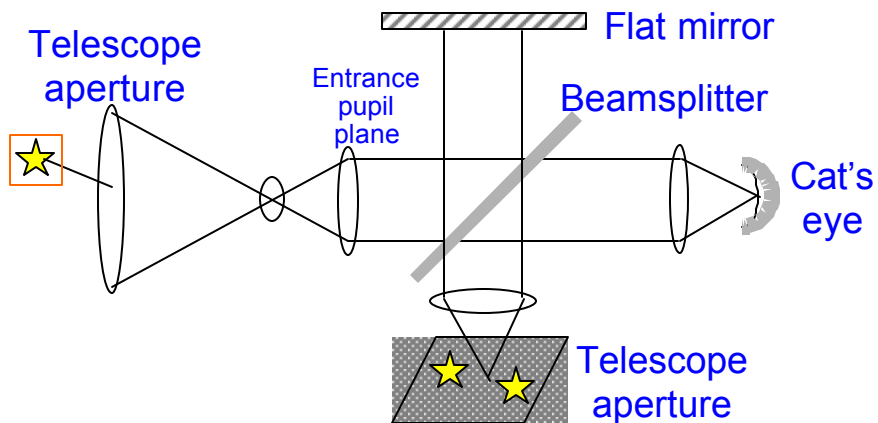


Figure 2.1-4 – The Nulling Coronagraph

2.1.4 Filter Wheel Coronagraph

Placing different masks and pupil shapes on wheels (as shown in Figure 2.1-5) at appropriate locations in the optical path can offer the flexibility of carrying several different coronagraph types in one spacecraft. This can optimize system performance for planetary searches around different types of stars located at different distances, and also permit astrophysics observations tailored to the object viewed.

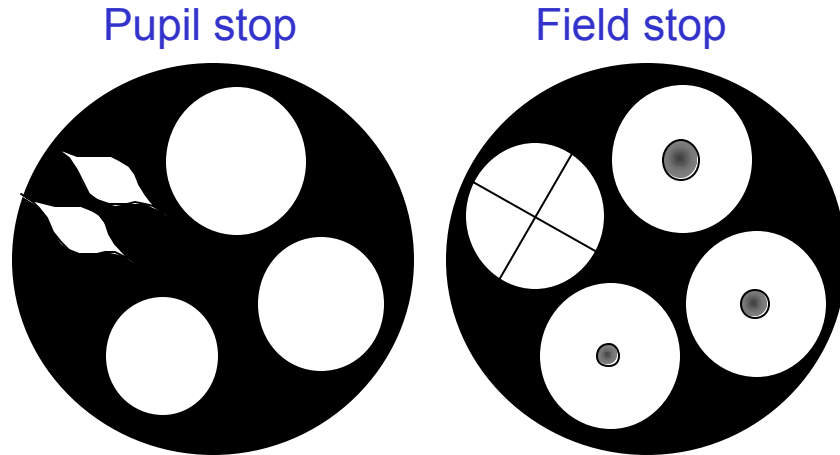


Figure 2.1-5 Pupil stop and Field Stop Filter Wheel Examples

2.1.5 Coronagraph and Outriggers

By adding smaller collector telescopes flying in formation with a large central coronagraph (as shown in Figure 2.1-6), the central unit can act both as a stand-alone coronagraph and as a combiner for a very large optical interferometer. The feasibility of such a system depends on the accuracy and controllability of positions and pointing angles in the formation. With a 100-meter formation diameter, and outriggers with apertures as small as 20 cm each, such a complex system could offer a variety of operating modes suitable for observing different-size target systems, and an imaging resolution as good as 2 mas. This type of system is similar to that proposed for the Planet Imager mission, and thus may demonstrate key dilute aperture technology.

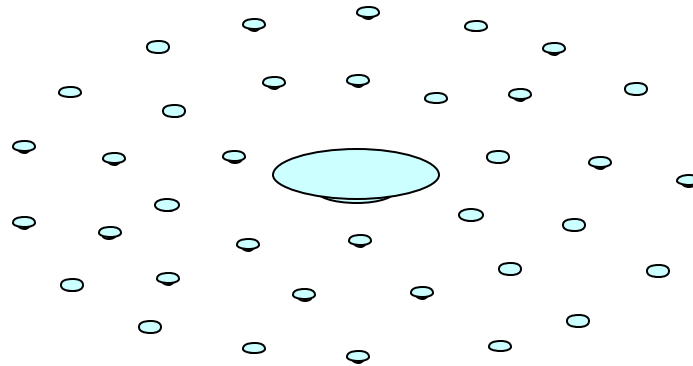


Figure 2.1-6 Coronagraph and Outriggers

2.2 *Emitted-Light Options*

The light directly emitted from planets in the habitable zone peaks at mid-infrared (MIR) wavelengths, typically around $10\ \mu\text{m}$. At these wavelengths the total starlight is only about 10^7 time brighter than the planet, as compared to 10^{10} for visible-light systems. Also, optical surfaces need not be as perfect as for shorter-wavelength visible-light systems. Unfortunately, the size of the diffraction angle increases directly with wavelength, so a sizeable aperture or baseline is needed to see planets close to the star. With near-term space technology this appears to rule out a single-aperture TPF operating in the MIR, but might permit a multi-aperture interferometric solution. We have studied 14 possible interferometer configurations, each offering a way to null the light from the star while gathering a varying signal from the planets near it. To do this, collimated beams relayed from the different apertures must be combined, with a half-wave delay in

some of them, so as to cause precise destructive interference for the starlight. An example of such beam combination is shown in Figure 2.2-1, taken from the design Ball Aerospace produced for the TPF “booklet” published in 1999.

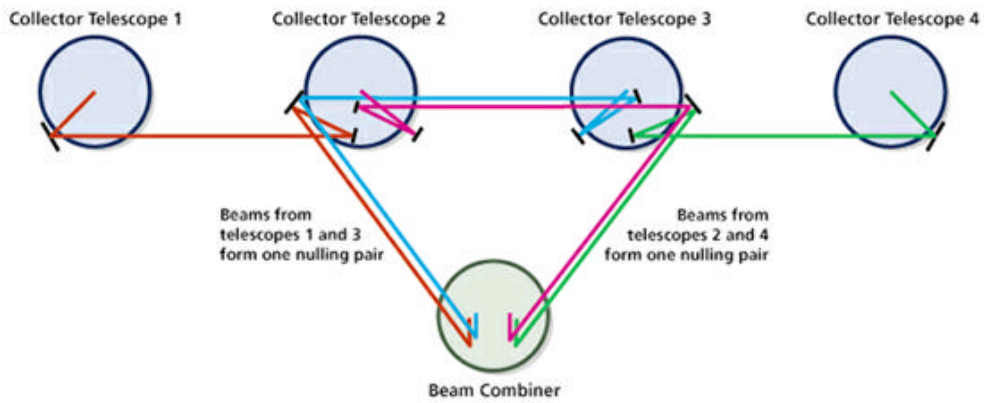


Figure 2.2-1 Beam Combination Example for a Multi-Aperture TPF Interferometer Concept

The half-wave delay component, which would be in the beam combiner subsystem, is shown schematically in Figure 2.2-2.

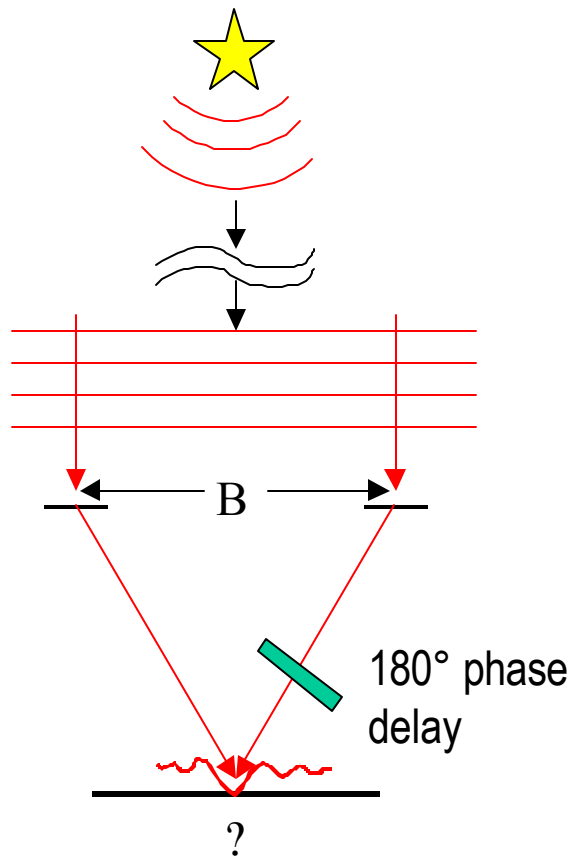


Figure 2.2-2 Phase Flip can suppress starlight by a factor of over 1 million

All our interferometer concepts involve collecting light from the entire planetary system on a single detector, thus they would be quite vulnerable to residual (i.e., after nulling) noise from the total incident

starlight, which for coronagraphs would fall mainly on different detector pixels than for the planet. The interferometric concepts will also be highly sensitive to exozodi noise, especially for systems with more dust emission than our own. Such noise would greatly reduce interferometric fringe visibilities and would complicate both the maintenance of the starlight null and the detection of the planet signal. Even local zodiacal emission would be a problem for these designs, for the same reason. Therefore, orbits which provide large fractions of time away out of the ecliptic plane might be preferable: our Princeton members have studied several such orbits.

The MIR coverage would optimally be from 7 to 24 mm, at spectral resolutions from 1 to 100. There are some good biomarkers in the MIR, with the capability to penetrate through dust to study protoplanetary disks and many shrouded astrophysical objects. However, MIR observations require cryogenic operation to minimize self-emission noise, which makes contamination from cryo-plating a major concern, especially if propellants are used for maneuvers.

If the interferometric TPF architecture has an adjustable baseline, this gives it a way to easily select the angular resolution appropriate for a given target. If this adjustability is achieved with several free-flying spacecraft, their separations can be large enough to offer very high resolution for astrophysics observations (e.g. 2 milliarcseconds fringe spacing for a 1000 m baseline at 10 micron observing wavelength). To construct images, however, the single-detector limitation requires substantial rotation and baseline adjustment, which can consume considerable time and fuel, but does at least offer the advantage of generating spectroscopic information simultaneously. (However, since the interferometric constructive-interference stripe lands fully on the planet for only one wavelength at a time, the efficiency of collecting imagery and spectra is decreased.) Fuel needs and resultant contamination (and stray light) can be minimized for a monolithic (single connected structure) interferometer, where reaction wheels using solar-electric power can provide the rotations, but such structures can generate detrimental vibrations, and their performance is hard to validate adequately during ground test.

The following are the emitted light options that seemed to have the greatest potential merit.

2.2.1 Interferometer – Full Monolith

A linear interferometer with 4 to 6 collecting apertures mounted on a structure up to 100 m long would require apertures each at least 3 m in diameter to accomplish the TPF mission; see Figure 2.2-3. The interferometric configuration would most likely best be a chopped dual double-Angel-cross (DAC), which combines the light from three apertures (one large central one, and two smaller outer ones) in two interleaved and offset groupings, with alternating views from each grouping permitting subtraction of nulled stellar signals so that the planet signal stands out more sharply. To do this, the starlight-suppressed ("dark") beams are combined with alternating ± 90 degree phase chopping. This requires exquisite control of the modulation symmetry: if the phase were off by even one degree, a large, false planet signal would be produced. Nulling would be accomplished with an achromatic combiner. This instrument would be designed to have thermal and stray-light shielding over its entirety, but its limited baseline would yield insufficient resolution to accomplish many of the astrophysics goals.

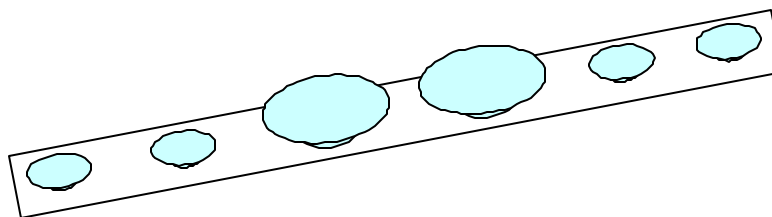


Figure 2.2-3 Interferometer Full Monolith

2.2.2 Free-Flying Chopping Linear DAC

This would be a similar configuration to that in 2.2.1, but would involve free-flying spacecraft with four to six collectors (averaging 3.5 m in aperture diameter) and a combiner/controller spacecraft, as shown in Figure 2.2-4. It would be a good instrument for high-resolution astrophysics at long baselines, but the repositioning time for the formation might be excessively long to provide adequate coverage of the u-v plane for astrophysics goals.

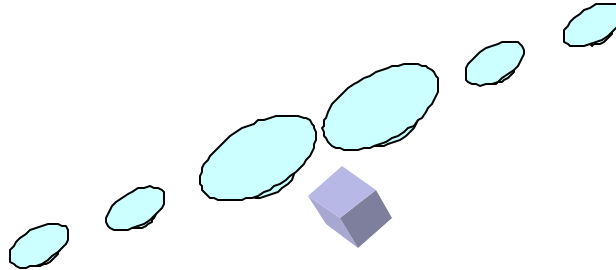


Figure 2.2-4 Free Flying Linear DAC

2.2.3 Laurance (“Super Darwin”) Interferometer

This is a larger-apertures version of the European Space Agency's concept for the Darwin mission. We feel that apertures of 3 m or larger are needed to achieve the entire TPF mission. We have a packaging concept for this which can fit within launch fairings expected to be available (see Figure 2.2-5). The free-flying spacecraft are arranged in a hexagonal configuration around a central combiner, which permits a formation rotation of only 60 degrees to sweep the interferometer fringes around the whole planetary system. This type of configuration might be expected to provide achromatic nulling at greater than a 10^6 reduction of starlight, which ought to enable slightly shorter observing times. It also provides robustness, because it can still function even if one collector is lost.

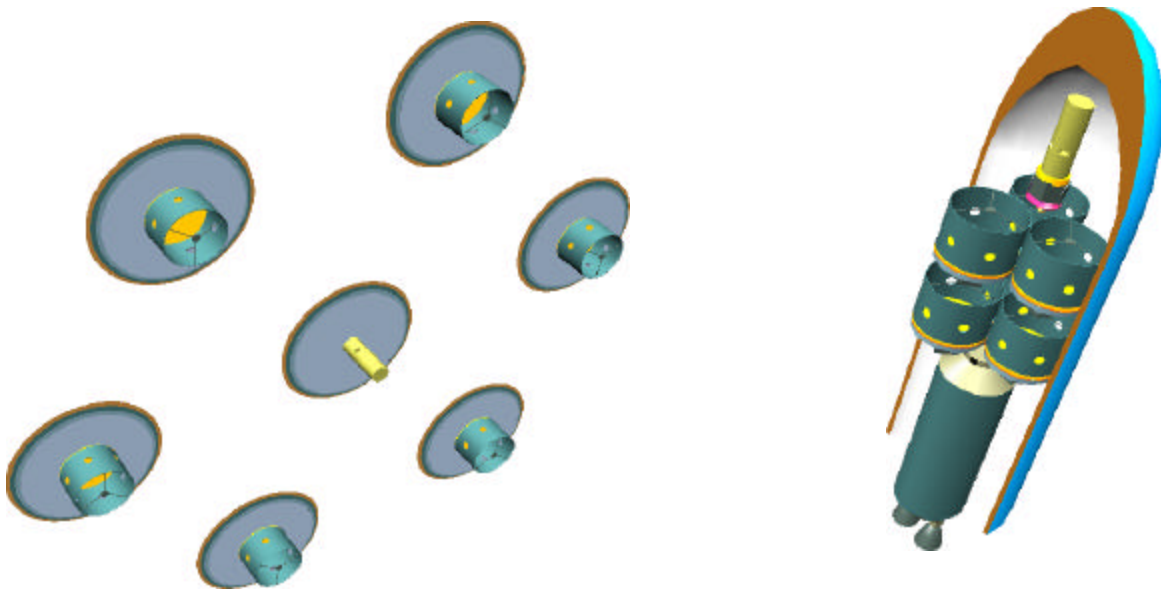


Figure 2.2-5 Laurance (Super Darwin) Interferometer -- Deployed & Launch Configuration

2.2.4 Darwin Mariotti Interferometer

As shown in figure 2.2-6, this is a different geometry than the Laurance configuration, and the collector beams are paired to permit Mariotti-type chopped nulling which may enhance phase closure for optimum chopping. However, that would be a complex process that doesn't cover all potential planet angles on the first try.

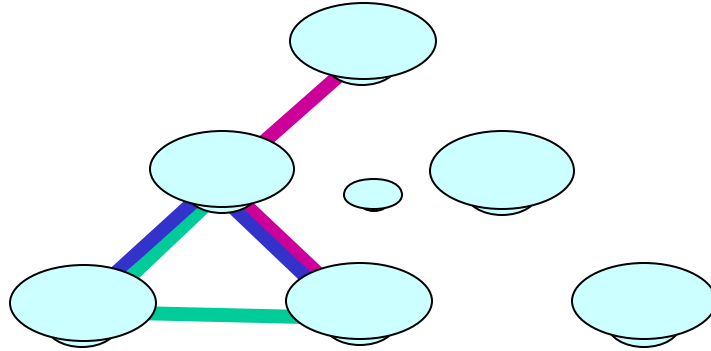


Figure 2.2-6 Darwin Mariotti Interferometer

2.2.5 Cable-Car Interferometer

Since the main problem with free-flying cryo interferometers would be contamination of optical surfaces due to the propellants used for repositioning, there are reasons to try for a monolith solution employing solar-powered reaction wheels to eliminate that likely contamination source, and permitting use of a single all-protecting thermal and light shield. However one large problem with monoliths would be the vibration present during data collection. Those factors led us to conceive of a system (Figure 2.2-7) which provided the advantages, but not the inadequacies, of both free-flyers and monoliths. This "cable-car" interferometer would couple the collectors to a long but lightweight (and not necessarily very rigid) structure during maneuvers and rotations. Then, during observations, the collectors would be decoupled from the structure but be held nearby, by micro-thrusters or possibly even magnetic sources. With the extensive use of mechanical devices to couple and decouple, there might be some risk of such a system providing long mission life.

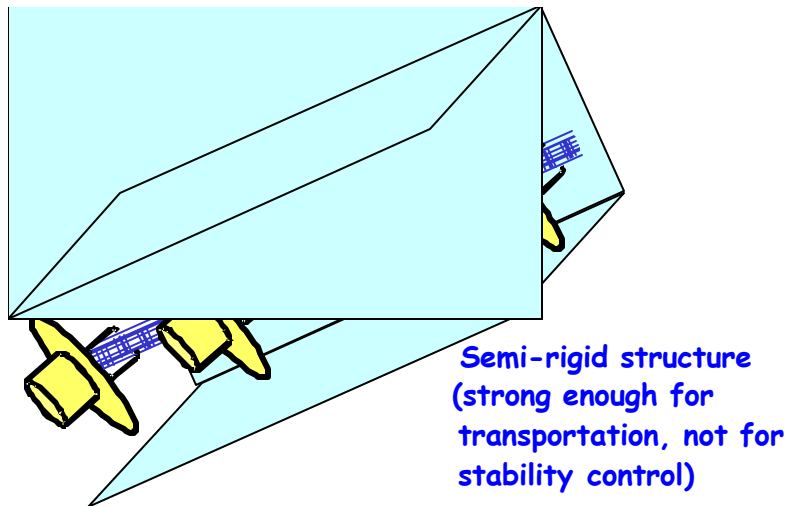


Figure 2.2-7 Cable-Car Interferometer

2.3 *Diversity Options and Their Limitations*

In our brainstorming sessions, we developed ideas for many other ways to detect extrasolar terrestrial planets. None of these directly detected extrasolar terrestrial planet photons, but they still offered ways to achieve detection of the planet's presence, and in one case perhaps even its chemical constituents. Some of these could estimate a planet's mass, some its cross-sectional area, and some its rotation period and seasonal or diurnal variations. Since they could not do the entire TPF mission set forth to us, we will just list the names of these "diversity" architectures here:

Gravitational microlensing, transit photometry, transit spectroscopy, secular variations, planet effects on exozodi, stellar astrometry, stellar Doppler shifts, and use of large ground-based telescopes with adaptive optics systems.

3 **Recommendations**

3.1 *General Comparison of Emitted and Reflected Options*

Having developed these and other less feasible options for the TPF mission, we again returned to the science and implementation aspects discussed earlier and attempted to compare the two families of instruments on those bases. For the MIR interferometer, planet searches would be at lower star-to-planet total contrast and might simultaneously be able to detect spectral features and measure planet temperature. A free-flying interferometer should have a better chance of achieving the resolution required to separate very closely spaced objects. Planet phase effects are expected to appear smaller to an IR instrument.

With mirrors working at longer wavelengths, a lower surface quality for each individual mirror is adequate. Similarly, there may be less sensitivity to micro-meteors, scattering and contamination (although greater potential for contamination in a cryo instrument). The flexibility of an adjustable baseline permits suitably matching the nulling region for many planet configurations.

One unusual factor deserving minor consideration is that a multi-spacecraft (free-flyer) interferometer design concept itself might be inherently fascinating and thus add even more to public interest in TPF.

On the other hand, the coronagraph has several features advantageous for science. Most important, it seems capable of achieving shorter integration times, by at least a factor of 3, as seen in Figure 3.1-1. Due to the way the coronagraph takes data, i.e., not having to reposition constantly, it can observe entire planetary systems more rapidly. It also provides good image resolution over a much larger FOV, viewing the outer regions of planetary systems, and yielding more astrophysical information. At visible wavelengths, confusion from background sources would be far less than in the IR, allowing for easier interpretation of the results. Information could be gathered from planet phases, and large cold planets could be seen. Finally, in case the instrument (sadly) fails to null starlight perfectly and detect nearby planets, the coronagraph option still provides an excellent and versatile space telescope and therefore would not be a total loss.

The coronagraph is a simpler system to deploy and operate. There is no need for a cryo system, it requires less propellant, and it has fewer surfaces to protect from contamination. It will very likely be of lower cost and need fewer new technologies developed – but above all will not need the precision constellation control required for a free-flying interferometer.

Architecture Option	?? ?m	IWD, mas	OWD mas	Airy rad., mas	Gaussian HW, mas	Lyot --	Pixel, mas	Integrat'n Time, Ks
Gauss-Lyot 8-m CG (Collecting area 50 m ²)	0.3	50	2000	8	100	.80	10	50
	0.5	50	2000	13	100	.71	18	10
	1.0	52	2000	26	104	.45	58	23
	2.0	104	2000	52	208	.45	116	180
Gauss-Lyot 16-m CG (Collecting area 200 m ²)	0.3	50	2000	4	100	.85	5	4
	0.5	50	2000	7	100	.80	9	1
	1.0	50	2000	13	100	.71	18	1
	2.0	50	2000	26	100	.41	63	12
TPF 1-2-2-1 Un-chopped IF 3.5-m x 75-m B/L (Area=38 m ²)	7	18	270	19	--	--	--	93
	10	26	390	27	--	--	--	33
	20	52	780	55	--	--	--	83
Dual DAC Chopped IF 3.5-m x 75-m B/L (Area=58 m ²)	7	16	270	19	--	--	--	230
	10	22	390	27	--	--	--	83
	20	44	780	55	--	--	--	200

Figure 3.1-1 Comparison of Integration Times for Detecting an “Earth” at 10 pc, at 1 AU, at Quadrature, with SNR = 5 at Spectral Resolution = 10

3.2 Judging Criteria

Reading the above comparisons, it is easy to see that a more systematic approach is necessary to arrive at a ranking of the options within each group. To do this, we returned to the original seven criteria we were asked to consider, in Figure 1.2-1 above. Choosing a total of 100 points for a perfect design, the points were assigned as equal weights of 25 points each for planet finding/characterization and astrophysical capabilities. Ten points each were assigned to the remaining 5 categories. The final values, shown in Figure 3.2-1 below, are clearly subjective and relative but they represent the best scientific and engineering judgment of our team at that time.

Arch.	Planets	Planets	Astroph.	Technol.	Cost	Risk	Rel./Rob.	Future	TOTAL
# Architecture Name	1 - Find.	1 - Char.	2	3	4	5	6	7	SCORE
1 Spergel var.-pupil corona.- 8 m	15	10	23	10	10	10	10	8	96
2 Masking coronagraph - 10 m	15	10	25	6	8	6	8	10	88
3 Nulling coronagraph - 10 m	13	8	20	4	6	4	6	8	69
4 Focal plane phase mask	9	5	10	6	6	4	6	5	51
5 Microtube block	0	0	0	0	0	0	2	0	2
6 Occulting Screens	2	2	1	0	0	0	5	0	10
7 Spergel pinhole screen	2	2	1	0	0	0	5	0	10
8 Interferometer Full-Monolith	3	8	10	4	4	4	5	2	40
9 Interferometer Lite-Monolith	2	4	6	4	6	4	5	2	33
10 Interferometer 2D Tethered	3	3	5	0	3	2	2	4	22
11 Interferometer Linear Tethered	2	2	2	0	3	2	2	4	17
12 Interf. FF - Chopping Linear DAC	5	7	20	6	7	6	6	8	65
13 Interferom. FF- Chop.Dual Bracewell	3	2	20	4	7	4	4	6	50
14 Interf. FF- Laurance Super-Darwin	7	9	23	6	5	6	6	10	72
15 Interferometer FF - Mariotti triangle	7	9	23	4	5	4	4	6	62
16 Interferometer FF - TPF-Lite	4	3	12	4	6	4	4	6	43
17 Interferometer FF - Fizeau	1	1	8	4	4	4	4	4	30
18 Interferometer FF - Hypertelescope	7	12	14	1	0	0	4	8	46
19 Interfer. FF - Mini - hypertelescope	1	1	4	2	5	0	2	6	21
20 Super-shielded Interferometer	7	9	20	0	1	0	2	6	45
21 Cable-Car Interferometer DAC	4	6	15	6	6	6	6	8	57
Points Possible:	15	10	25	10	10	10	10	10	100

Figure 3.2-1 Comparison of All TPF Architectures

No candidate concept receiving a zero in any category was included in the final list, which reduced the number of options from 30 to 21. For each criterion, one of the architectures was given the maximum score, as the highest performer. The architectures labeled in blue are the highest scoring and so were chosen to be the selected architectures for this exercise.

3.3 Final Selections and Rationale

At this early stage of architecture development, these candidate designs appeared to have some promise.

3.3.1 The Spergel Pupil Coronagraph

This instrument concept was our first choice. It has a novel and powerful way to search quickly for “Earth-like” planets and characterize them. This design can easily accommodate a wide variety of astrophysical instrumentation and appears to be the most cost-effective of the options proposed. We developed this concept most fully, and present here some of its characteristics.

For a Spergel-pupil coronagraph with an 8-m aperture, Figure 3.3-1 shows our initial calculation of the integration times required for detection (SNR = 5) of an Earth-mass planet (with albedo = 0.5, independent of wavelength) orbiting a solar-type G star. In the figure, the green, thick black, light blue and red lines represent 3000, 10,000, 30,000, and 100,000 second integrations. With a 10,000 second integration, we should be able to detect planets in the habitable zones out to 20 pc around G stars.

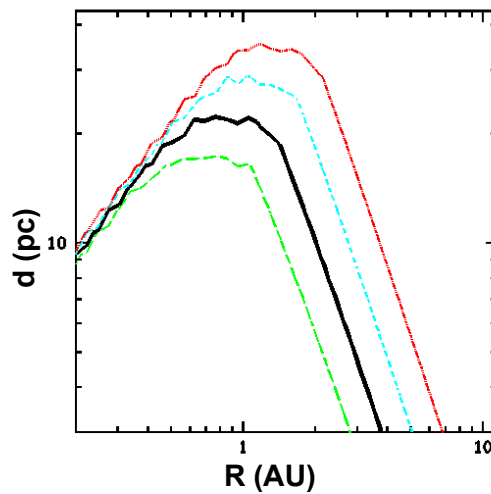


Figure 3.3-1 Predicted "Earth" Detection Limits: 8m-Aperture Spergel-pupil Coronagraph

A view of a notional concept for the spacecraft implementation of the Spergel-pupil coronagraph is shown in Figure 3.3-2. To be launchable in fairings expected to be available in the TPF time frame, both the off-axis secondary optics and the stray-light baffle tube will be deployable. We expect the primary mirror to be on the order of 4 meters by 8 to 10 meters, of monolithic construction but possibly assembled from smaller segments to form a nearly rigid surface, controllable with about 300 actuators to compensate for low-spatial-frequency distortions. There will be a deformable mirror to correct mid-spatial-frequency wavefront error, and a large focal plane detector array to enable viewing wide fields, including full planetary systems, but especially useful for astrophysics observations.

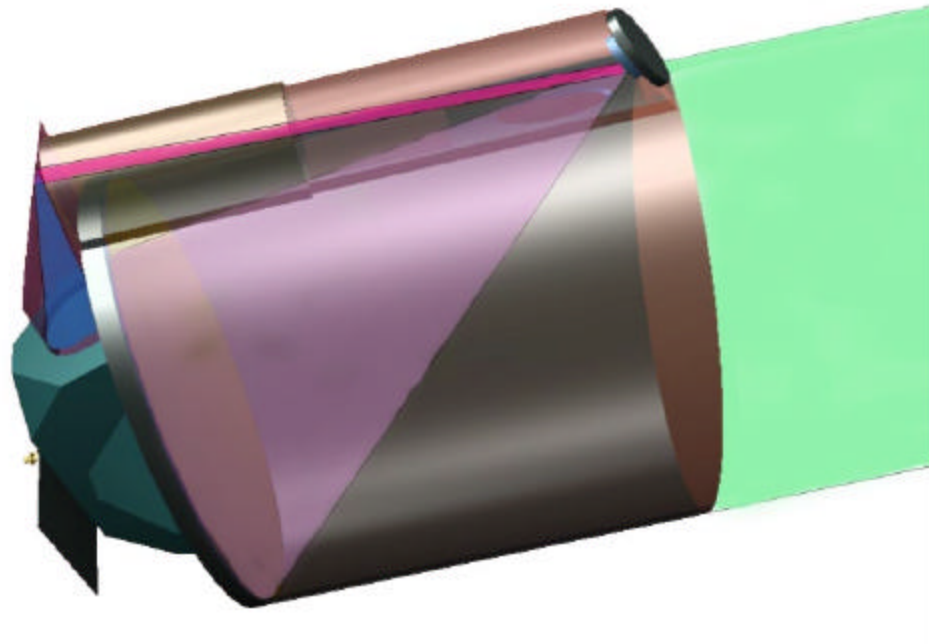


Figure 3.3-2 Design Concept for Spergel Pupil Coronagraph Spacecraft

3.3.2 The Super Darwin Interferometer

This ranks high due to the uniqueness of the technology, an approach entirely different from that of the coronagraphs, and therefore one which might have a chance of succeeding if the coronagraph options prove to face some insurmountable technical challenge. It requires larger collectors and hence a larger launch vehicle than the Darwin Book design and therefore could be very costly. As with all free-flyer interferometers, it has an adjustable baseline which can be adjusted to give the best performance for each planetary system, and offers very high resolution if it will work well at long baselines. Controlling the entire constellation of spacecraft to required positional and attitudinal accuracies represents a major technical challenge.

3.3.3 The Masking Coronagraph

This shares the advantages of a visible light system and its very large mirror, and might permit searching for planets more rapidly, and possibly closer to their stars (than with a Spergel-pupil coronagraph) by looking at image positions interior to the edge of the gradient mask. If a filter wheel configuration houses a variety of mask dimensions and shapes, an optimum mask could be selected and inserted for each planetary system viewed. An additional advantage of this type of coronagraph is that it has been most thoroughly studied and modeled already, and represents therefore a minimum of unknown technology. Manufacturing the mask to the tolerances required for the TPF mission may produce the greatest risk, next to that of maintaining adequate wavefront control.

3.3.4 The Chopping Linear DAC Interferometer

Possibly the most cost-effective of the free-flying interferometers, it is not as robust as the Darwin book design and probably would take too long to search for 150 planets, so it might do for a de-scoped TPF mission. It would take a long time to do synthesis imaging, because of the need to re-position all the spacecraft and to cover adequately the u-v plane.

3.3.5 The Cable Car Interferometer

This is an unusual “long-shot” concept that may stimulate a variety of breakthrough technologies. It provides a way to take advantages of the re-pointing capabilities of a large monolithic interferometer (using power, not propulsion), while during data collection still supplying the same freedom from structural stresses and vibrations as a monolith interferometer.

3.4 Summary of Recommendations

Unexpectedly, we found that visible-wavelength coronagraphic options appear to offer the greatest apparent observing efficiency for detecting and characterizing potential nearby terrestrial planets, including observing important biomarkers. Generally the coronagraph options held a speed advantage of at least a factor of 3 over the interferometers. That could mean detecting over 3 times as many planets during the mission. In addition, a very wide range of important astrophysical observations are possible with coronagraph architectures.

The coronagraph options promise greater robustness for detecting planets in systems with large amounts of zodiacal dust. For the interferometer the exozodi signal all falls on the sole detector, along with the planet signal. As a result, the required integration time is dominated by the exozodi levels; the relevant relation is close to linear: 10 x zodi requires 10 x integration time. At present the quantity of exozodiacal dust around other solar systems is poorly known. Ground interferometers will eventually measure exozodi levels down only to less than approximately ten times that in our solar system. (At visible wavelengths, zodi signals and planet signals are roughly the same, but both are nearly matched by the diffraction leakage and scattered light from mirror irregularities, so increases in zodi have relatively minor impact. Total effective background in the visible remains smaller than in the IR, and the visible wins with shorter integration time.)

A major consideration is the likelihood that an effective TPF visible-light coronagraph option would have a life-cycle cost much less than for equally capable MIR interferometer options. The main reasons for this difference are shown in Figure 3.4-1.

Cost Factor	Emitted-Light	Reflected-Light
Space Element Instrument Spacecraft Bus Integ. and Test (system-level) Launch Vehicle	IR/cryo Beams, OPD, nulling Many (for free-flyers) (Cryo/multiple testing) Atlas V/Delta IV	One-telescope cheaper Less tech. development One Less integ. and test Atlas V/Delta IV
Ground Element Infrastructure Operations	More processing power More complex maneuvers	
Science Efficiency		Lower cost per planet

Figure 3.4-1 Life-Cycle Cost Comparisons (Green = Advantage, Red = Disadvantage)

Fewer development and implementation risks are expected for the visible-light coronagraph options when compared to the MIR interferometer options. The main risk factors are shown in Figure 3.4-2.

Risk Factor	Emitted-Light	Reflected-Light
Cost	Beam and contamination control, cryo	1-telescope cheaper
Technology	Technology program now in place	Less technology development
Adequate testing	Separated instruments	Easier to test
Schedule	Multiple instruments	Large monolith mirror
On-orbit failures	Contamination levels	Easier to service

Figure 3.4-2 Comparison of Risks for Two Families (Green is Lower, Red is Higher)

An overall summary of the advantages for each family is shown in Figure 3.4-3

Family Element	Emitted Light – MIR (Interferometers)	Reflected Light – Vis./NIR (Coronagraphs)
Science	Lower total star-planet contrast Planet spectral features (possibly) Planet temperature measures Planet phases less variable Angular resol. of discrete objects Penetration, viewing MW, other dust Little overlap with ground scopes	Lower risk of confusion impact Imaging quality over wide FOV Images and spectra capture rate Information in planet phases Can see cold large planets Upgradeable to multi-uses, UV Simultaneous astrophys. & planets
Implementation	Technology for future IR IFs Lower surface quality needed Adjustable baseline – match planets Less sensitive to scattering, contam. Less sensitive to micrometeorites Design interests and inspires public	Simpler deployment No need for constellation control Less propellant, contamination No cryo systems Fewer new technologies Lower cost and risk

Figure 3.4-3 Family Advantages Matrix (Green = Major Advantage)

However, the challenges of extremely accurate wavefront control for suppression of scattered starlight, and manufacture and deployment of a very large aperture might make implementation of a TPF coronagraph more difficult in practice than building one of the types of infrared interferometers previously considered the best candidates for doing the TPF mission. Therefore, to give the greatest chance of really accomplishing the mission we truly felt the best solution would be to continue to study and develop the technologies in both architecture families. This process should include defining precursor missions both for space demonstration and to acquire science data, such as information on the density of typical exozodi

disks and on the statistical likelihood of observing planets. The space missions would likely involve smaller instruments than could perform the full TPF mission, in either or both the coronagraph and interferometric technology categories.

REFERENCES

D. N. Spergel, "A New Pupil for Detecting Extra Solar Planets," <http://xxx.lanl.gov/pdf/astro-ph/0101142>, posted in 2001

N. J. Kasdin, D. N. Spergel, and M. G. Littman, "An Optimal Shaped Pupil Coronagraph for High Contrast Imaging, Planet Finding, and Spectroscopy," (submitted 2002)

M. J. Kuchner and W. A. Traub, "A Coronagraph with a Band-Limited Mask for Finding Terrestrial Planets," *The Astrophysical Journal*, May 2002 (in press)

Ball Aerospace TPF Architecture Study Part 2 -- Final Architecture Study

1 Architecture Definition

1.1 Coronagraph Architecture Overview

In Phase Two of the TPF Architecture Study, the Ball team concentrated on its highest-ranked concept from the initial architecture phase, a visible-light coronagraph. This concept appears to be a viable and relatively low-cost approach to meet the scientific objectives of TPF. A single large telescope with a light-collecting area of about 30 m² is needed to complete both the planet search and astrophysics observations in the allotted five-year mission time.

1.2 Optical Design Approach

As for any challenging optical engineering design, we began by establishing the performance requirements and flowing them down to the optical system and subsystems. Next, we identified the main engineering uncertainties and implementation challenges, and created a baseline design to minimize these and to serve as a starting point for our analyses. We studied two main design sub-classes for the visible-light coronagraph, the "shaped-pupil" (SP) and the "classical" (CL) options. Each can be implemented within the current baseline optical design, and can even be implemented as compatible configurations selectable on orbit. Both have a single entrance aperture, an image plane mask (coronagraphic field occulter, or CFO), and a subsequent camera, and require that an extremely accurate and stable wavefront be achieved and maintained.

1.3 Optical System Description

We describe first the common elements of our two coronagraph options. The primary mirror is a 4 x 10 m ellipse with a 14.9 m focal length. It is an off-axis segment of an 11 m diameter paraboloid. The essential elements of both our coronagraph options are shown schematically in Figure 1.3-1.

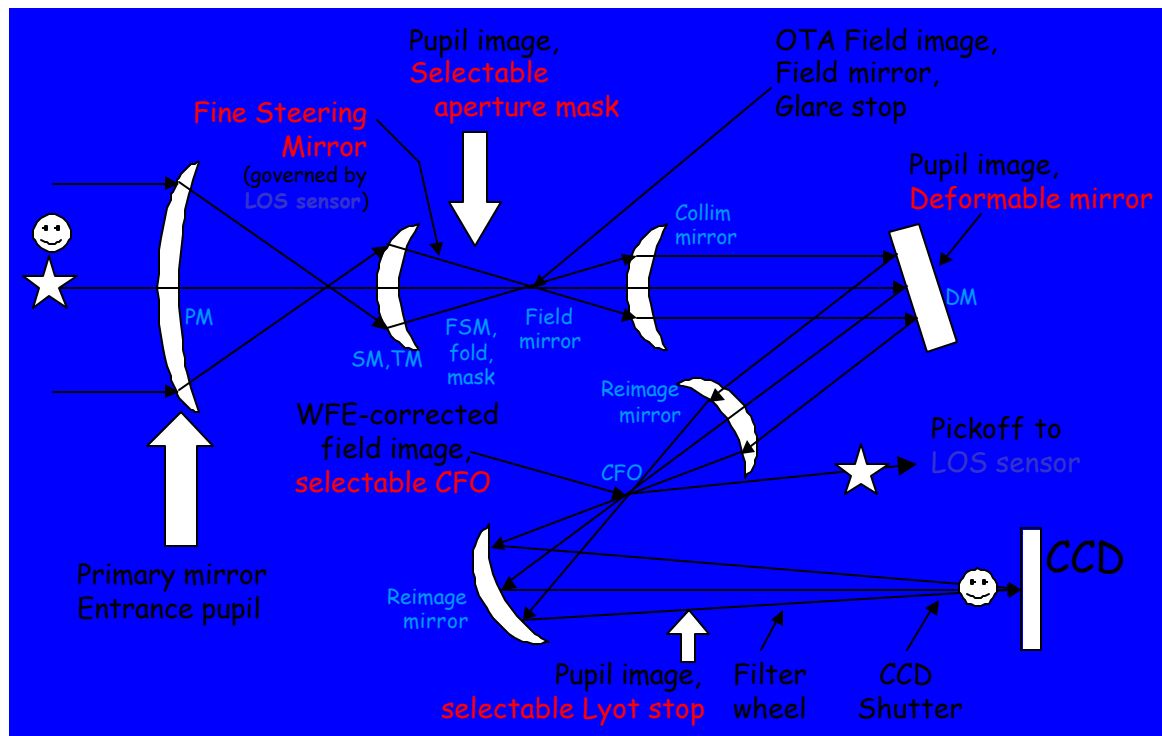


Figure 1.3-1 Optical Elements for Shaped-Pupil and Classical Coronagraph Options

1.3.1 Shaped-Pupil Coronagraph

This option is a novel type of coronagraph which uses the shape of the primary mirror (actually a mask later on) to suppress its own diffraction. (The shape of this entrance-pupil mask is designed so that its diffraction pattern has strongly-suppressed sidelobes in two quadrants of the sky surrounding the star.) The primary mirror is not apodized, and a binary mask at the first pupil image provides this novel diffraction suppression. The CFO is a binary mask, whose purpose is just to block the bulk of the excess light, whereas the CFO in a CL coronagraph acts more subtly as a filter. There is no Lyot stop. Wavefront corrections are made with actuators on the back surface of the primary mirror (low spatial frequencies only), and with a 256 x 100 actuator deformable mirror (DM) at a later pupil image.

The entrance pupil mask has a prolate spheroidal function shape, as shown in Figure 1.3-2. It is a binary mask, with an opaque outer region, and one or more transparent (empty) inner regions. The intensity requirements are that the opaque portions must have transmission $<10^{-7}$. If this requirement is achieved, there are no phase requirements there. The requirement on the shape is a boundary accuracy of <1 micron for a 10 cm mask. We are investigating the option of using actuators to control the shape of the mask, in order to mitigate the effect of small amplitude errors (see Section 2.3.1).

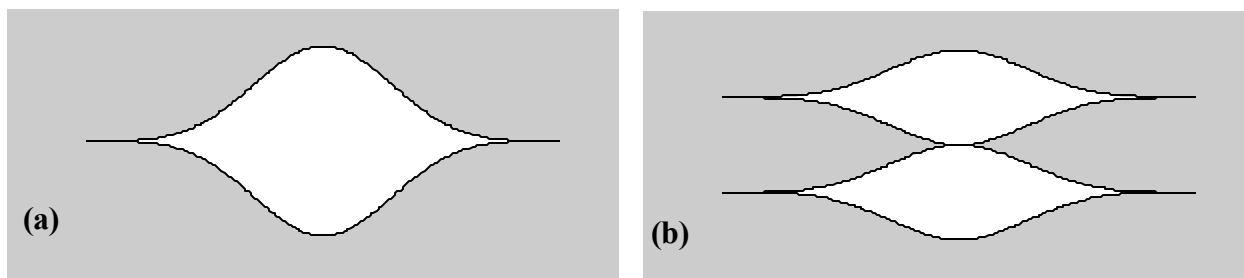


Figure 1.3-2 Shaped pupil masks: (a) single aperture mask; (b) dual-aperture mask with the same collecting area and IWD but a wider region of sky within which planets would be detectable (especially in the narrow "waist" in Figure 2.6-1)

The image plane mask (CFO) is also a binary mask. The rejection of diffracted starlight is achieved entirely with the pupil plane mask – starlight is diffracted into two regions (roughly opposite quadrants) of the image plane. The purpose of the image plane mask is only to remove most of this light, to avoid problems with stray light and detector saturation downstream. Therefore, the requirements for shape and intensity are rather loose – several microns for shape, and transmission $<10^{-4}$.

The outer radius of the effective field of view is set by the number of actuators on the deformable mirror. It is approximately 1.5 arcseconds at a wavelength of 700 nm. The inner radius is set by the ability to suppress diffracted starlight in our search quadrants. For a wavelength of 700 nm, this is 70 mas. Both radii scale with wavelength, so that we can achieve 50 mas inner radius in our preferred observing band of 450-550 nm.

Our requirements for pointing jitter are 14 mas in body pointing, with control by a fine steering mirror to 1 mas. Our requirements on vibrations depend on their frequency and location. Their effect on the wavefront must be controlled to <50 pm rms.

A small number of pupil plane and image plane masks can be chosen for different types of targets/observations. Our design does not require changing the pupil mask, but a selection of field occulting masks allows us to optimize the inner working distance (IWD) — the minimum angular separation from a star at which an Earth-like planet can be detected — for a given wavelength.

1.3.2 Classical Coronagraph

The optical architecture is a coronagraph with a non-apodized primary mirror, and no pupil mask. There is a graded image plane mask, plus a Lyot stop. Wavefront corrections are made with actuators on the back surface of the primary mirror (low spatial frequencies only), and with a 256 x 100 actuator deformable mirror at a pupil image.

There is no entrance pupil mask in this design. The CFO will be very long in one direction (so it has zero bandwidth in that direction). This choice provides ~15% greater throughput than the spot-like mask case, and makes the instrument insensitive to pointing errors and wavefront intensity and phase errors along that direction. The cost is a small fraction of the search area (reducing it from 100% to 85%).

In the other direction, the CFO will be band-limited to a ~20% bandwidth (see Kuchner and Traub 2002), with a Gaussian mask as a backup in case the band-limited mask proves to be too hard to manufacture. (Our numerical simulations were made assuming the Gaussian mask, which is, in fact, more conservative.) The attenuation for the CFO must be $>10^6$ at the center, assuming that we use a graded Lyot stop. The *rms* transmission error must be $< 10^{-8}$ over the core of the stellar image at critical spatial frequencies. Elsewhere on the mask, the tolerances are 2-6 orders of magnitude less severe. The design is completely insensitive to high spatial frequency transmission errors — those with a period $< \lambda/2D$ (equivalent angle on the sky), where D is the primary mirror diameter.

The CL coronagraph can achieve a smaller Inner Working Distance than a SP coronagraph. However, a variable transmission mask (required for the CL coronagraph) is more challenging to produce, whereas the binary masks of the SP coronagraph are comparatively easy to manufacture.

The outer radius of the effective field of view is set by the number of actuators on the DM, and is approximately 1.5 arcseconds at 700 nm wavelength. The inner radius depends on our image plane mask-Lyot stop pair, and is a soft limit – the transmission of a Gaussian mask drops as the angular radius decreases (note that a planet's brightness *increases* with decreasing orbital radius). Our nominal image plane mask - Lyot stop pair (which was used for the calculations reported here) consists of an attenuation HWHM of 3.3 Airy radii, and a Lyot stop which is an elliptical aperture with the same aspect ratio as that of the primary mirror, but with a size that blocks 50% of the light. If we define the 30% transmission point through such an image plane mask as our IWD, then $IWD = 59 \text{ mas} \approx 0.00059 \text{ arcsec}$ (microns).

For our operations scenario, we have the option of a small number of image plane and Lyot masks which can be chosen for different types of targets/observations. By using a smaller (sharper falloff) image plane mask, we can achieve a smaller Inner Working Distance. However, we then need to block more of the light with the Lyot stop, reducing the total throughput.

The throughput factor for the image plane mask will depend on the separation angle between the star and the planet (see Section 2.2). We specify a Gaussian mask, with a HWHM of 3.3 Airy radii. In practice, this has almost no effect for 1 A.U. planets at 3 or 5 pc, but a substantial effect for 1 A.U. planets at 10 or 15 pc.

1.4 Spacecraft and Observatory Overview

The instrument is built around a monolithic Primary Mirror that utilizes a very low diffraction, off-axis design (see Figure 1.4-1). The observatory has a 5 year design life, with expendables (e.g. fuel, batteries) sized for 10 years. The system uses adaptive optics to control wavefront error in a set-and-forget mode. The baseline orbit is an arrested drift-away orbit, although several other orbits are under consideration. The spacecraft has a launch mass of ~6,000 kg and could be directly inserted by a Delta IV Heavy launch vehicle.

The telescope has a large baffle and an articulated sun shield. The baffle and sun shield control thermal gradients in the optical system during an entire planet observation sequence. The spacecraft is three-axis stabilized. Spacecraft attitude control is to 10 mas (1sigma, cross-axes), using FGS (Fine Guidance Sensor) and RWA (Reaction Wheel Assembly) control. Instrument pointing control to 1 mas is achieved with a Fine Steering Mirror. The articulated sun shield balances solar torque (Cp to Cm offset) so as to minimize attitude control disturbances to the system. The RWA can therefore operate in a relatively narrow, optimized speed range. The propulsion system utilizes simple hydrazine components. Higher ISP (lower mass) options were not required, but may be examined in the future.

The thermal design provides accurate control over primary mirror temperature variations. The spatial variations (over a maximum 24-hour observing cycle) are controlled to within 0.03 °C. Active heater control of the optical bench is required to accomplish this design. The primary mirror operating temperature of 0 °C was chosen to minimize dimensional changes of the ULE, Zerodur optical components. This operating temperature also simplifies Manufacturing Testing & Calibration.

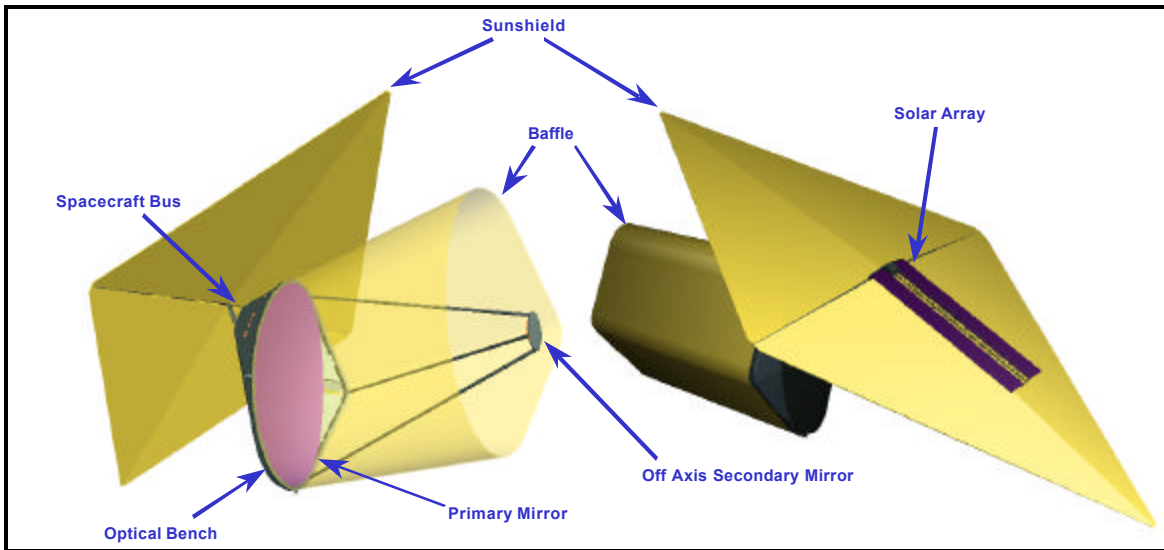


Figure 1.4-1 Observatory Major Features

The power subsystem is capable of 2.1 kW EOL (End of Life). The power system will take advantage of the rapidly maturing lithium-ion battery technology, as well as the growth in solar cell efficiencies. The telecommunications system utilizes the Deep Space Network (DSN) 34m ground stations, with Ka-Band for downlink of scientific information (maximum data rate of 8 Mbps), and X-Band for downlinking of spacecraft engineering telemetry (5 kbps). The C&DH (Command and Data Handling) software will utilize existing standard methods currently employed on spacecraft.

1.5 Opto-mechanical Configuration

The coronagraph will require some very large precision structures and mechanisms. The major elements are illustrated in Figure 1.5-1. The 4.2 meter primary mirror is supported by a composite iso-grid optical bench. In addition to supporting the primary mirror, the optical bench supports deployment struts for the secondary mirror. The fold mirror is supported from a deployable support structure. Ancillary optics, as well as the science instruments, are supported on the backside of the optical bench. Low mass, precision deployments, and dimensional stability during observations will be the driving mechanical requirements for this subsystem.

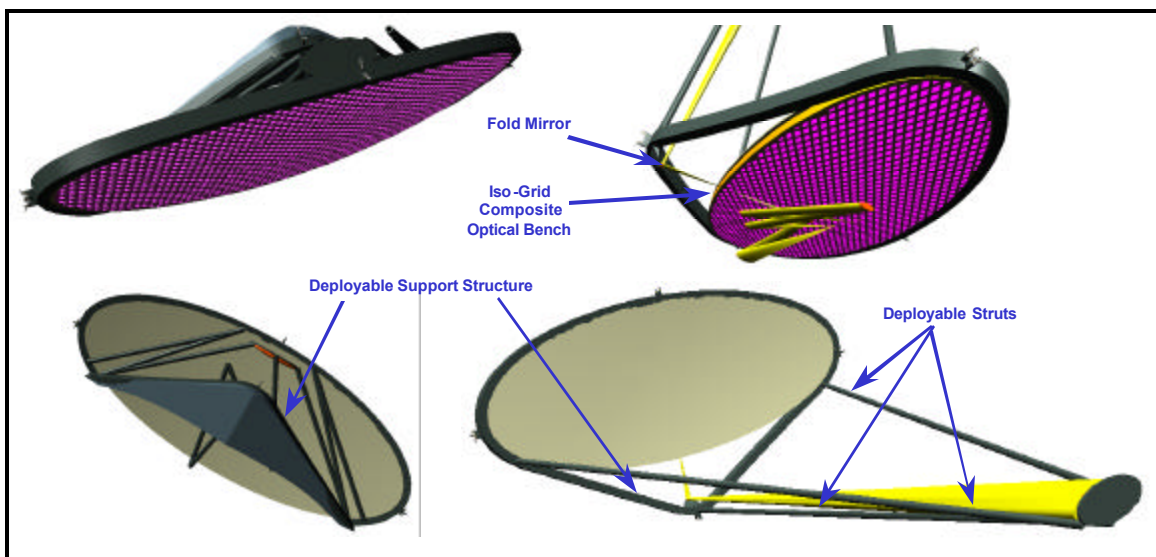


Figure 1.5-1 Opto-mechanical Features

1.6 Shielding

A large deployable baffle and sunshield are major elements in controlling thermal loading and stray light. These elements are shown in Figure 1.4-1. Minimizing spatial temperature variations of the optical elements over a maximum 24-hour observing cycle is a major challenge for the coronagraph. The use of an articulating sunshield and baffle are highly effective in controlling these variations (see Figure 1.6-1). These shields will build on the technology developed for the NGST sunshield. Future options to be investigated will include inflatable, shaped-memory, and conventional deployment mechanisms.

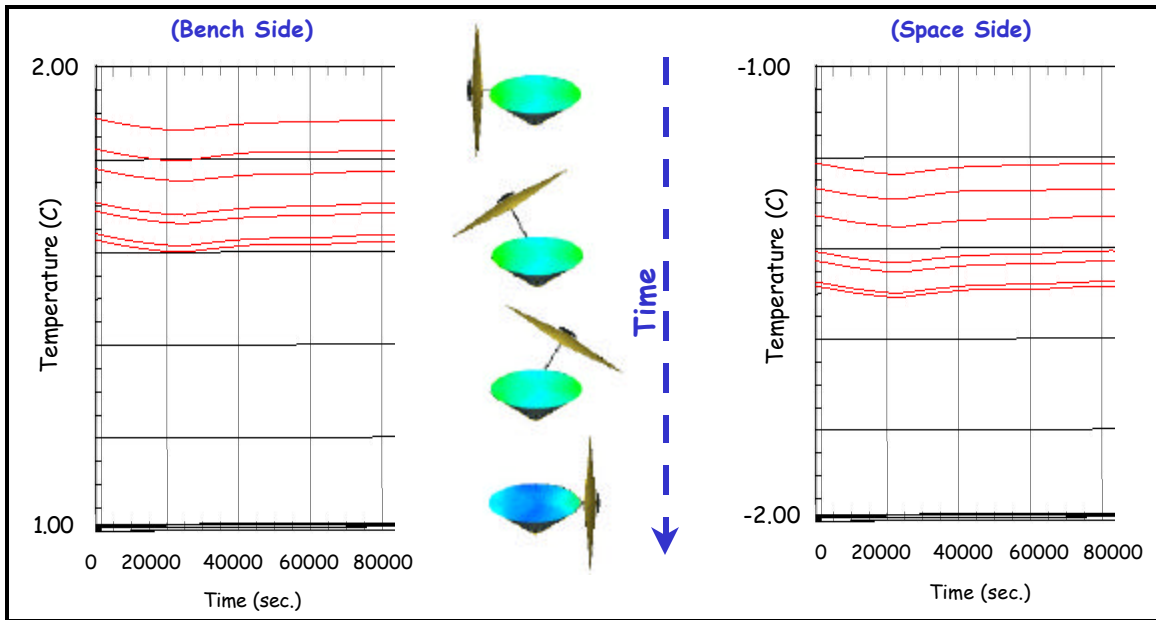


Figure 1.6-1 Thermal Shielding Temporal Gradient Effects

1.7 Orbit Options

There are several possible orbits for the coronagraph. They include L1 halo, L2 halo, drift away, arrested drift away, and distant geocentric orbits (See Figure 1.7-1). The arrested drift away orbit was chosen as the baseline, but the other orbits need to be considered in greater detail as the observatory design continues to evolve in the future. Figure 1.7-2 summarizes the advantages and disadvantages of the potential orbits.

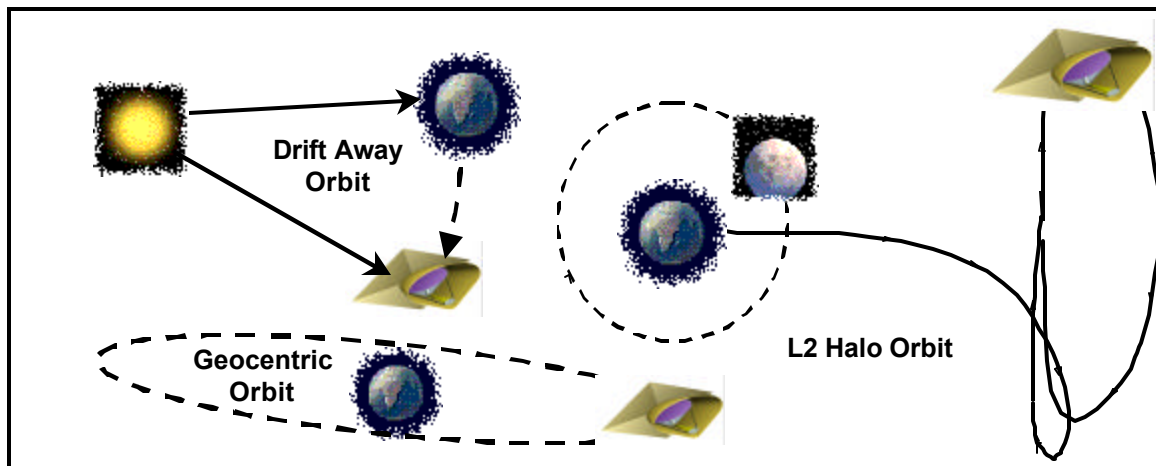


Figure 1.7-1 Orbit Options

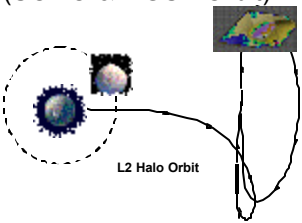
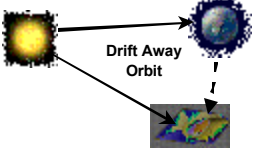

Orbit	Advantages	Disadvantages
L1 or L2 Halo (SOHO & NGST Orbit) 	Large Sky Coverage NGST Ground Compatibility NGST Ops Compatibility Low Insertion Energy $C3 = -0.69 \text{ (km}^2/\text{s}^2)$	Station Keeping $C3 = -0.7 \text{ (km}^2/\text{s}^2)$ Direct $C3 = -2.2 \text{ (km}^2/\text{s}^2)$ Lunar Swing-by
Drift Away (or <i>Modified</i>) (SIRTF Type Orbit) 	Minimal Disturbances No Eclipse Large Sky Coverage No Station Keeping	Moderate Insertion Energy $C3 = 0.3 \text{ (km}^2/\text{s}^2)$ Large Telecommunications Distance at End of Life <i>Modified:</i> $C3 = 0.3 \text{ (km}^2/\text{s}^2)$ 220 m/s of ΔV to arrest drift
Distant Geocentric Orbit (Distant Retrograde Orbit) 	Minimal Disturbances No Eclipse No Station Keeping Closest to Earth - Autonomous Servicing option Comparable to L2 Insertion $C3 = -1.85 \text{ (km}^2/\text{s}^2)$	Sky Coverage (TBD) Preliminary Findings Needs More Optimization

Figure 1.7-2 Orbit Trade Summary

1.8 Launch Strategy

Our concept is launched with a single EELV (Evolved Expendable Launch Vehicle). The baseline utilized a Delta IV Heavy launch vehicle, but the design is intended to be compatible with other EELVs. Ariane 5 and Atlas V are also potential launch vehicles for TPF. Figure 1.8-1 summarizes the launcher capabilities.


ELV	Escape Capability (kg) $C3 > 0.3 \text{ km}^2/\text{sec}^2$ (Direct Insertion to Drift Away Orbit)	Notes
Delta IV (4050-H19) (Baseline)	9,255	 1st Flight 2003, large margin
Ariane 5 (AR5E)	7,250	Evolved Version of AR5G, under development
Atlas V 551	6,300	1st Flight 2002, provides minimal margins

Figure 1.8-1 Launch Vehicle Summary

It should be noted that the Delta IV Heavy has additional performance margin and volume for larger TPF concepts. While the 10 ? 4 meter coronagraph is sufficient for the current science requirements, we also explored a 13 ? 4 meter option that is compatible with Delta IV Heavy capabilities. The shuttle was not considered for several reasons. The shuttle is very expensive, it requires a boost stage for orbit insertion, and it may be retired or replaced by the

time TPF launches. If a viable RLV (Reusable Launch Vehicle) emerges from the NASA Space Launch Initiative program, it will also be considered for TPF.

2 Planet Detection Capabilities

2.1 Performance Factors

The two key parameters which characterize the performance of a TPF architecture are: (1) the IWD and (2) the integration time required for detection. Although both of these quantities depend on the type of star and on the exozodiacal light level ("exozodi level"), they depend to first order on two mirror parameters. The length of the long axis of the mirror sets the minimum Airy radius (12 mas at 500 nm for our 10 m long mirror), and this in turn sets the scale of the IWD. The area of the mirror sets the scale of the sensitivity. Our design requires ~30 m² mirror area, achieved with a 4 m minor axis.

2.1.1 Diffraction By The Primary Mirror and Entrance Pupil Masks

In an ordinary telescope, diffraction by the apertures causes the greatest amount of stellar leakage — starlight which is spread into off-axis pixels of the detector, including those where the planet might reside. Coronagraph-specific features, such as the field occulter and Lyot stop or the peculiar shaped-pupil mask, are designed to suppress this diffraction contribution. The desired factor of suppression of this off-axis leakage constrains some key parameters in the design of the coronagraph; these parameters in turn govern the IWD and the effective collecting area.

Classical coronagraphs traditionally have been made with a Gaussian-profile CFO (a mask in the image plane that blocks the image of the star). This CFO and the Lyot stop constitute a sophisticated filter for optical waves; they work together to suppress the on-axis starlight and the off-axis light due to diffraction by the rim of the primary mirror. A useful innovation of the Ball team is band-limited mask designs, which offer improved suppression by clever tailoring the beam to match the Lyot stop.

Another innovation by our team is the shaped-pupil approach (Kasdin, Spergel, and Littman 2002), a radical alternative to the classical coronagraph. In the shaped-pupil design, the diffraction of the aperture is carefully structured to cancel in some regions of the image plane; i.e., the wings of the point spread function are suppressed along certain directions in the image plane.

2.1.2 Scatter From Wavefront Errors

After the diffraction contribution has been adequately suppressed in the region of the planet, the next most important stellar leakage contribution is wavefront scatter, which is due to small ripples of wavefront error. In a good telescope these are small enough to produce an ordinary astronomical image of high quality, but can still scatter enough starlight into the planet pixels to overwhelm the planet flux there. For TPF, the wavefront must be improved by a factor of several hundred, relative to that adequate for diffraction-limited imaging, in order to achieve sufficiently rapid and convincing detection of earthlike planets.

The most important scatter contribution comes from phase profile error in the beam, specifically at the final image of the entrance pupil before the CFO. This wavefront error is approximately the sum of wavefront errors on all the preceding mirrors. This creates a pattern of speckles (small light patches) in the final image which can obscure the planet. Similarly, the amplitude profile can have errors in it, for example from reflectivity variations across the surface of each mirror. This creates another pattern of speckles in the final image.

Though the two speckle patterns come from different sources, they can add coherently. Thus, within certain limitations, one can generate an intentional phase profile error whose speckles cancel the speckles of an amplitude profile error. The main limitations are that if only one deformable mirror is used (a) the speckle reduction is only possible over half of the final image — e.g., only the "left" half — and (b) this works only over a narrow optical passband. Though by this principle we can compensate a residual amplitude error using the DM, in practice this will still require an excellent initial amplitude profile, and may require narrowing the spectral window for a given observation. The best approach for setting amplitude profile requirements and dealing with the residual errors is not yet understood. Some discussion of the issues appears in Section 2.1.3 below.

2.1.3 Setting Requirements for Stellar Leakage and Other Backgrounds

The main challenge in coronagraphy is the suppression of stellar and other backgrounds in the planet pixel and their time variation. We characterize these backgrounds by a parameter Q , which is the planet flux (or a typical value for it) divided by the background flux in the same pixel. (Higher Q is good, because it means that more of the measured light is planet light.)

Any steady flux from scattered or diffracted starlight will bring with it statistical noise, which just comes from the randomness of arrival of individual photons. This noise will obscure the tiny flux from the planet, until the instrument can gather enough photons to distinguish a real excess flux due to the planet from a random excess due to this noise. This part mainly affects the integration time of each observation.

In a similar way, time variation of the background signal in a pixel can obscure a planet signal. The significant background contributions in a planet pixel are (a) the residual light from aperture diffraction; (b) the speckle from amplitude profile errors; (c) the speckle from phase profile errors; and (d) the light from exozodiacal dust in the vicinity of the planet. Of these, (c) is most vulnerable to time variation, (a) is next, and (b) and (d) are the least vulnerable. The last item on the list (d) is the one we cannot affect with instrument design. As it happens, the levels of local zodiacal light (function of ecliptic latitude) and exozodiacal light (depends on the unknown level of dust and unknown disk inclination angle of the other planetary system) will affect the integration time only slightly, because they make a modest contribution to the background in the planet pixel.

During the study, we originally set our requirements based on the goal of reaching $Q=1$, i.e., total background per pixel equal to the typical planet flux of 10^{-10} of the stellar flux. This is a very stringent requirement, and the result is some difficult requirements on the amplitude and phase profiles, and also more than 50% throughput loss in either the Lyot stop or due to the shaped-pupil. We might relax these challenging requirements by allowing some background contributions to be higher than the planet flux ($Q<1$) as long as we can trust them to be stable. (An additional consequence of this relaxation is that the required integration times will increase.) For example, we may be able to tolerate a larger amplitude profile error, because that error, however large, will remain stable for days. But we must recognize that this will tighten requirements for stability of other errors such as in the phase profile. If the amplitude profile error doubles, the other stellar leakage errors must be a factor of 2 more stable. This area needs further study, to find the right balance of speckle brightness and stability.

2.2 Coronagraph Inner and Outer Working Distances

Suppression of light at small angular separations from a star is the key challenge of a coronagraph. We have performed numerical simulations of the diffraction performance of our optical designs. For the SP architecture, the starlight leakage drops sharply out to 50 mas (at 500 nm wavelength), reaching a leakage level of 3×10^{-11} there. We cannot detect any planets (even bright ones) at smaller angular separations, but the throughput is the same at 50 mas as at much larger angles. The leakage drops slowly at angles beyond 50 mas.

With our CL coronagraph design, such a “cliff” does not exist – the leakage varies more smoothly with angular separation. With the Gaussian image plane mask described above (HWHM of 3.3 Airy radii), the leakage level reaches 10^{-10} at 32 mas (500 nm wavelength). However, the image plane mask causes the throughput to fall sharply with decreasing angular separation in this region, so that only bright planets can be detected inside 50 mas.

The number of actuators in our Deformable Mirror (256 along the long axis) sets the maximum spatial frequency that we can control on the wavefront. The resulting Outer Working Distance is 1.1 arcseconds for both architectures, assuming a minimum of 3 DM actuators per cycle and $\lambda=500$ nm. Giant planets in a Jovian orbit (5 A.U.) will be detectable for stars *beyond* 5 pc.

2.3 Wavefront Error, and Control With The Deformable Mirror

Achieving $Q_{\text{scatter}} \geq 1$ requires stringent wavefront purity. We will use a Deformable Mirror (DM) to perform high accuracy (0.07 nm *rms*) correction of the wavefront at critical spatial frequencies (3 – 80 cycles across the aperture's major axis). Below 3 cycles per aperture, the requirement is 1 nm *rms*. Actuators on the primary mirror will be used for correction at low spatial frequencies to accuracies of a few nm. Stability and control of a DM at the

required precision have been demonstrated in ground laboratories. Greater concerns are stability of the rest of the optical system and knowledge of the wavefront error, which is needed in order to achieve accurate control.

A calibration sequence will be performed for wavefront measurement and correction. A series of exposures on a bright calibration star will allow off-axis scattered light levels to be measured. The DM will be adjusted to reduce the off-axis light after each exposure. This process will 1) take a substantial amount of time (perhaps a few hours), and 2) cannot be performed during a science exposure, since it requires use of the science camera. Therefore, the DM will be locked after the calibration step, and the challenge is to maintain the wavefront accuracy during a set of science measurements.

2.3.1 Amplitude Uniformity and Control With The Deformable Mirror

The goal for intensity uniformity of the starlight beam profile at the DM is 1.5×10^{-4} *rms* in the critical spatial frequency range. If we can achieve this goal, then the DM will be used only for correcting wavefront phase, and we will be able to perform planet searches in two opposite regions (approximately quadrants) of the image plane. If we can't achieve this level of intensity uniformity at the DM, adjustments with the DM can be used to correct the intensity over half the image plane, giving one usable quadrant. In this latter case, our search times for planets will increase by a factor of two.

2.4 Thermal Distortion and Control

The greatest challenge to maintaining a precision wavefront during multiple hours of science measurement is likely to come from thermal effects. Our mirror has very low areal density, and its thermal inertial will be low. Our primary approach to minimizing temperature changes is to use a large sunshield – this will keep the radiation environment nearly constant during the hours (and multiple azimuths) of observations on a given star. Construction of the telescope mirror out of Ultra Low Expansion (ULE) glass will minimize the effects of residual temperature changes on the mirror figure.

Furthermore, our design/observing strategy is insensitive to two types of thermal effects. First, a spatial gradient (or, more generally, any spatial variation) is acceptable if it is constant in time. The spatial variation will result in a warped mirror shape, but the calibration procedure that sets the DM will correct for it. Second, a spatially uniform change in the mirror temperature with time will cause little or no warping. We will only be affected by the double-differenced variation: temporal changes in the spatial temperature gradients.

Although these design characteristics will keep thermal effects at a low level, we have not yet done sufficient quantitative analysis to compute Q_{scatter} for realistic observing scenarios.

Our nominal plan is for purely passive thermal control of the optical elements. However, active control is a fallback option. Local heaters would be required, driven either by input from local temperature sensors, or by a global thermal model.

2.5 Vibration Effects and Control

Although vibration would seem to be a very serious problem for precision wavefront control, in two ways it is easier to handle than thermal distortion. First, vibrations are generally of much higher temporal frequency, so that the resulting amplitudes are small, and damping is favorable. Second, vibrations will be largely due to “point” sources (e.g. reaction wheels), allowing the use of isolators to greatly reduce their effects on the optical structures.

We levy two requirements on the effects of residual (post-isolation) vibration levels. First, the wavefront tilt (pointing error) must be <0.5 mas (1 mas for the SP coronagraph). Second, the wavefront distortions at critical spatial frequencies must be <0.05 nm *rms*.

Optical-mechanical modeling of our structure, using model HR0610 reaction wheels and Honeywell 1.5 Hz isolators, showed that both these requirements can be met (Figure 2.5-1).

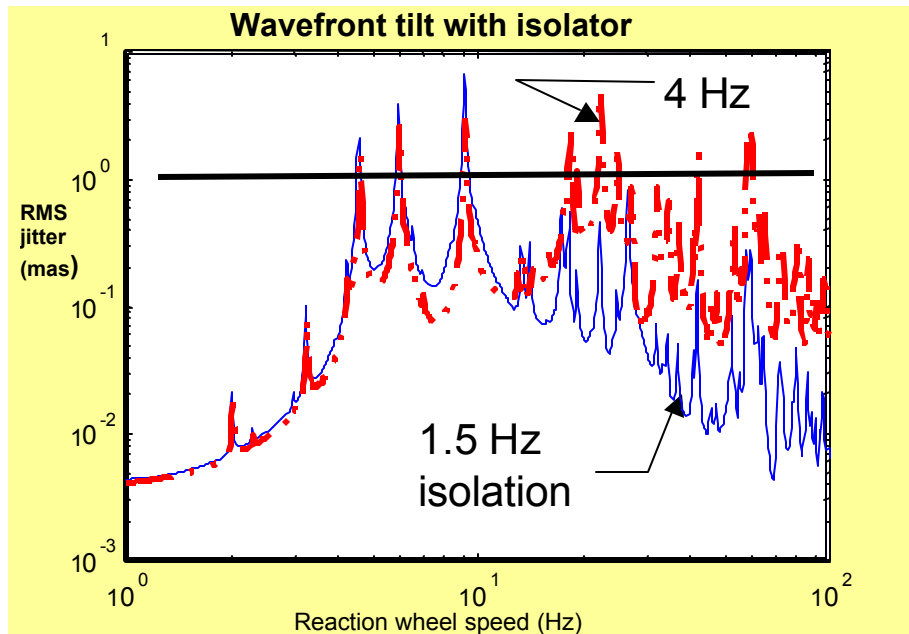


Figure 2.5-1 Results of Opto-Mechanical Modeling Show Adequate Control of Vibration

2.6 Homework Problem Results

Performance calculations with uniform assumptions (“ground rules”) were made by each team for its architecture. We give an overview of the results of these calculations here.

2.6.1 Broadband Detection of Earth Analogs Around Sun-Like Stars at Various Distances

In this exercise, we calculated detection times for the Earth at 1 A.U. around a sunlike star at various distances (3, 5, 10, and 15 pc), and with various levels of exozodiacal emission (multiples of 0.5, 1, 2, 5, and 10 compared to the level in our solar system). Observations at 700 nm were specified.

2.6.1.1 Calculation of Signal

Calculation of the count rate from the planet requires only the input spectral flux (matched to measurements of the Earth), the instrument throughput, and the instrument passband. To adhere to the guidelines, we chose a passband of 650-750 nm, with the 700 nm reference wavelength at its center, and the approximate bandwidth for which we get the optimum combination of sensitivity and rejection of starlight. (The system can operate at a 500 nm center wavelength for improved Inner Working Distance.) The instrument throughput consists of the area of the primary mirror (31.4 m^2), the fraction of light passed by the various masks (0.44 for the SP coronagraph; <0.50 for the CL coronagraph, depending on angular distance from the star), two reflections off aluminum coated mirrors and eight reflections off silver coated mirrors ($0.882^2 \cdot 0.988^8 = 0.71$), and quantum efficiency of the detector (0.80 at 700 nm).

2.6.1.2 Calculation of Noise

There are several noise sources. The statistical ones can be readily calculated with a spreadsheet.

At visible wavelengths, the statistical noise sources are: local zodiacal light, exozodiacal light, detector read noise, and detector dark current. Zodiacal light contributions used the supplied model of the emission in our solar system. For the local zodi contribution to represent the median value over the whole sky, an ecliptic latitude of 30° was assumed. The inclination of the distant solar system was set at 45° , so we get an extra factor of $\sqrt{2}$ in the exozodi contribution. The total received zodi flux is thus proportional to $1 \cdot Z \cdot \sqrt{2}$, where Z is the exozodi level, in units of the level in our solar system [note that the term of 1, from the local zodi, is the product of 0.5, due to our location in

the middle of the disk, and $1/\sin(30^\circ)$]. In addition to this algebraic factor and the specified spectral flux density, we need to account for the footprint of our coronagraph beam on the other solar system. This footprint is typically 0.1 to a few tenths of an AU in diameter, and accounts for the comparatively weak sensitivity of a coronagraph to the exozodi level (an interferometer is affected by the exozodi over most of the disk). Because surface brightness is independent of (non-cosmological) distance, the received exozodiacal flux is also independent of distance. (With the classical coronagraph, the graded image-plane mask causes sensitivity to be dependent on angular separation, and therefore also on distance to the planetary system.)

We assumed a CCD read noise of 2 electrons, and 0.001/s dark current, per pixel. We also assumed nine pixels per diffraction beam.

The systematic noise can be broken down into two components. The diffracted light is due to the finite size of the mirror, assuming perfect optical figure. The scattered light is due to imperfect optics (wavefront error). The residual diffracted starlight level was calculated with numerical simulations, based on the mirror size, observing wavelength, and nominal (i.e. design) characteristics of the masks (image plane mask and either a pupil mask or a Lyot stop). We define Q_{diffract} as the ratio in a pixel of planet flux to calculated residual diffracted flux, as given in the tables below. We levy a requirement of $Q_{\text{diffract}} > 1$ to enable planet detection. This requirements leads to our IWD – the point where star leakage is brighter than the planet.

We assumed that the scattered light level was equal to the planet flux level ($Q_{\text{scatter}}=1$). A straightforward analysis leads to the 0.07 nm wavefront accuracy requirements given in Section 2.3. We used a medium-fidelity wave propagation model of the scattered-light level, which incorporates wavefront errors but not amplitude profile errors. Obviously, a high-fidelity integrated model of wavefront error is needed to develop confidence in the performance.

With these values for the noise levels, we calculated the integration time required to reach S/N of 5.

2.6.1.3 Angular Search Range

With an ideal classical coronagraph with a circular aperture, the full 360° of azimuth around the star can be searched for a planet with a single exposure. However, both of our candidate architectures have azimuth restrictions. For the classical coronagraph, the 2.5:1 elliptical mirror limits our ability for searching small angular separations to approximately two opposite 90° azimuth spans. Therefore, we need two “pointings” to cover the full azimuth range.

With the SP architecture, the azimuth range is a function of angular separation from the star. Figure 2.6-1 below shows the level of starlight suppression at 500 nm wavelength for a Spergel/Kasdin dual shaped pupil. The use of a higher number (>2) of shaped pupils will increase the azimuth range of starlight suppression, but this has not yet been quantified for the region of small angular separations (50-100 mas). The azimuth range of high starlight suppression ranges from approximately 12° near the 50 mas IWD to 76° beyond 120 mas. With a symmetrical region on the opposite side of the star, the number of pointings needed to cover the full 360° azimuth range varies from 15 at 50 mas to 3 at angles >120 mas. The narrow useful azimuth range at small angular separations is the most serious performance drawback that we have identified for the shaped pupil coronagraph. This performance weakness can be mitigated by further subdividing the pupil (more sections, each of which is narrower), and is compensated by the much simpler technology of the binary masks used in this architecture, compared to the precision graded image plane mask required by a CL coronagraph.

If we are unable to achieve our required 1.5×10^{-4} intensity uniformity (which also affects the amount of scattered light) before the DM, and decide to use the DM to modify the intensity profile, we will only achieve our target starlight suppression on one side of the star. Therefore, the instantaneous azimuth range would drop by a factor of two, and we would require twice as many pointings (and approximately twice as much time) for a planet search.

We assumed a slew + settling time of 1500 seconds for each repointing.

2.6.1.4 Results

Figures 2.6-2 and 2.6-3 below give the total observing time required to achieve SNR=5 on a nominal Earth-like planet at the specified distances (d) and exozodi levels (Z).

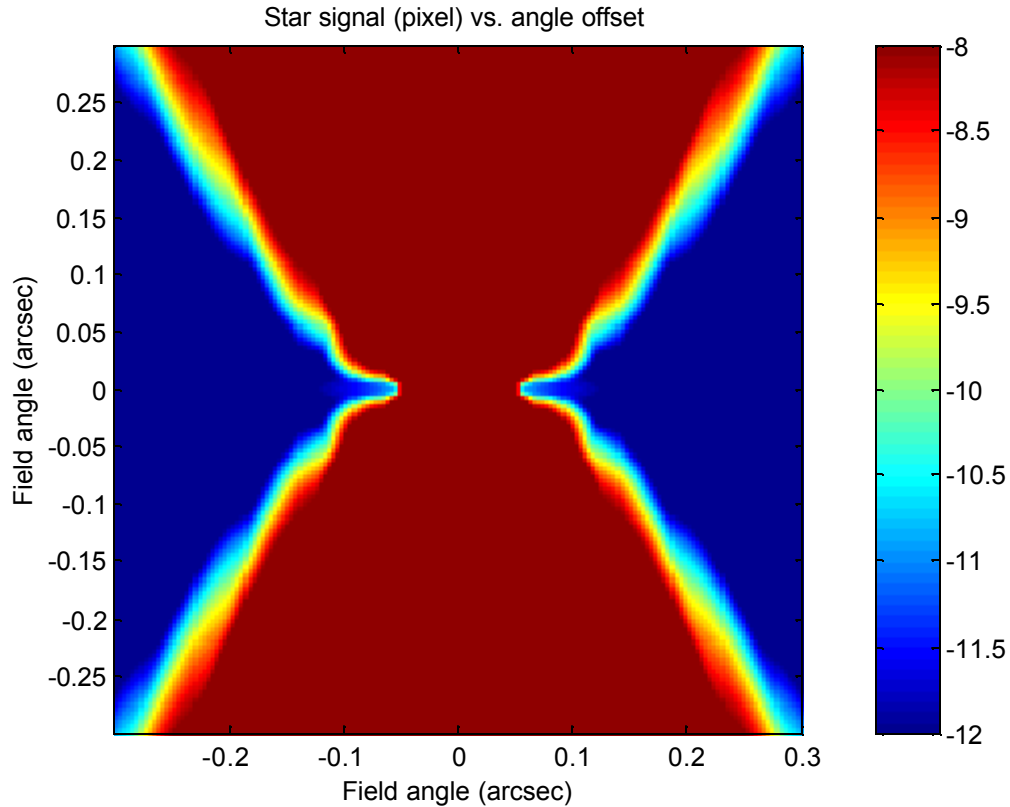


Figure 2.6-1 Starlight Suppression, $\lambda = 500$ nm, for Spergel/Kasdin Dual SP Mask. The blue areas are suitable for planet detection, while the reddish-brown areas contain residual starlight more than 100 times as bright as a terrestrial planet

For the SP architecture, the integration times are less than one hour for the 3 and 5 pc cases. At 10 pc, the total integration times are in the 5-9 hour range. For observations at 500 nm, the azimuth search range at 100 mas star-planet separation is substantially larger, and the total integration times at 10 pc are a factor of ~ 2 smaller than in Figure 2.6-2.

Results for 650-750 nm Shaped Pupil									
Total counts from local + exozodi in beam footprint (s^{-1})									
0.1503	0.2126	0.3371	0.7106	1.3332					
Z=0.5	Z=1	Z=2	Z=5	Z=10					
Total Integration time to get S/N=5 with slews and repointings (s)					d (pc)	Counts from planet (s^{-1})	Number of pointings	Q from diffraction	Q from scattering
1592	1593	1595	1603	1616	3	1.4482	2	200	1
3406	3421	3450	3542	3702	5	0.5213	3	150	1
18327	19080	20621	25391	33515	10	0.1303	9	20	1
Detection not possible					15	0.0579			1

Figure 2.6-2 SP Coronagraph Search Performance Table

For the CL coronagraph, we assumed an image plane mask with an HWHM of 3.3 times the Airy radius. Because of the image plane mask, throughput depends on angular separation from the star. Integration times are under one hour for the 3 and 5 pc cases, and 1-2 hours for the 10 pc case. At 15 pc, integration times are 3-8 hr at 700 nm.

Results for 650-750 nm Classical Coronagraph										
Total counts from local + exozodi in beam footprint (s⁻¹)										
Z=0.5	Z=1	Z=2	Z=5	Z=10	d (pc)					
0.150	0.213	0.337	0.711	1.333	3					
0.150	0.213	0.337	0.710	1.333	5					
0.133	0.187	0.297	0.627	1.176	10					
0.092	0.130	0.207	0.436	0.817	15					
Integration time to get S/N=5, including multiple pointings and slews (seconds)					d (pc)	Counts from planet (s⁻¹)	Number of pointings	Q from diffraction	Q from scattering	
1582	1582	1584	1590	1600	3	1.6457	2	20	1	
1742	1750	1765	1813	1895	5	0.5923	2	10	1	
2953	3101	3402	4331	5913	10	0.1306	2	3	1	
8041	9163	11441	18380	30044	15	0.0404	2	2	1	

Figure 2.6-3 CL Coronagraph Search Performance Table

2.6.2 Spectroscopic Search for Atmospheric Gases in Detected Planets

After computing broadband detection times for sample planets, we calculated the detection times for the 940 nm water line and the 760 nm molecular oxygen line, both assumed to be present at terrestrial abundances.

2.6.2.1 Calculations in Spectral Search

Because of our interest in the 940 nm water line, with the need for a continuum measurement on the long side beyond 1 micron, a CCD detector is not feasible. We chose an InGaAs detector, with quantum efficiency of 60% at 700 nm, 70% at 900 nm, 80% at 1100 nm. For atmospheric detection, the 940 nm water line will be observed with a spectral resolution of 24. For a biomarker search, the 760 nm molecular oxygen line will be observed with a spectral resolution of 70. A dispersing prism is assumed, with a throughput of 90%. For the 940 nm H₂O line, we measure two continuum channels: 1.010-1.057 microns, and 0.858-0.891 microns. These are not adjacent to our line channel – we “skip” one channel on either side of our line channel, in order to avoid the wings of the line. For the O₂ line, we measure four continuum channels (spanning 0.769-0.791 microns and 0.738-0.758 microns), two on either side of the line. These channels are adjacent to our line channel. Our algorithm for determining a detection is simple – we subtract the flux in the line channel from the average flux in the continuum channels. The diffracted and scattered light levels were calculated as for the broadband search case. Figure 2.6-4 gives the integration times required to reach S/N of 5 for the 940 nm H₂O line, with the shaped pupil coronagraph. For distances of 3 and 5 pc, the integration times are less than one hour. At 15 pc, the Inner Working Distance of the shaped pupil coronagraph is larger than the star-planet angular separation (67 mas), and we cannot do the measurement.

Results for 940 nm H₂O line, Shaped-Pupil Coronagraph										
Total counts per channel from local + exozodi in beam footprint (s⁻¹)					Number of continuum channels	Spectral Resolution				
Z=0.5	Z=1	Z=2	Z=5	Z=10						
0.078	0.110	0.175	0.369	0.693	2	24				
Integration time to get S/N=5 (seconds) with R=24					d (pc)	Planet counts (s⁻¹) in line	Planet counts (avg) in continuum	Q from dif-fraction	Q from scattering	
301	310	329	388	488	3	0.1201	0.4802	100	1	
965	1041	1194	1665	2468	5	0.0432	0.1729	50	1	
6465	7742	10324	18148	31257	10	0.0108	0.0432	10	1	
detection not possible					15	0.0048	0.0192		1	

Figure 2.6-4 SP Spectral Performance Table (1)

Figure 2.6-5 gives the integration times required to reach S/N of 5 for the 760 nm O₂ line, again with the shaped pupil. As with the 940 nm H₂O line, we cannot achieve adequate suppression of diffracted starlight to make the measurement for the 15 pc case.

Results for 760 nm O₂ line, Shaped-Pupil Coronagraph									
Total counts per channel from local + exozodi in beam footprint (s ⁻¹)					Number of continuum channels	Spectral Resolution			
Z=0.5	Z=1	Z=2	Z=5	Z=10					
0.013	0.018	0.029	0.061	0.114	4	70			
Integration time to get S/N=5 (seconds) with R=70					d (pc)	Planet counts (s ⁻¹) in line	Planet counts in continuum (avg)	Q from diffraction	Q from scattering
2553	2600	2696	2986	3473					
8071	8445	9196	11468	15292	5	0.0201	0.0427	150	1
51476	57599	69890	106940	168895	10	0.0050	0.0107	20	1
detection not possible					15	0.0022	0.0047		1

Figure 2.6-5 SP Spectral Performance Table (2)

Figures 2.6-6 and 2.6-7 give the corresponding results for the classical coronagraph.

Results for 940 nm H₂O line, Classical Coronagraph									
					Number of continuum channels	Spectral Resolution			
Z=0.5	Z=1	Z=2	Z=5	Z=10					
						2	24		
Integration time to get S/N=5 (seconds) with R=24					d (pc)	Planet counts (s ⁻¹) in line	Planet counts in continuum (avg)	Q from diffraction	Q from scattering
266	273	288	333	410					
858	918	1038	1409	2041	5	0.0487	0.1946	10	1
9835	11933	16161	28939	50309	10	0.0085	0.0339	3	1
100458	131724	194335	382337	695779	15	0.0022	0.0088	2	1

Figure 2.6-6 CL Coronagraph Spectral Performance Table (1)

Results for 760 nm O₂ line, Classical Coronagraph									
					Number of continuum channels	Spectral Resolution			
Z=0.5	Z=1	Z=2	Z=5	Z=10					
						4	70		
Integration time to get S/N=5 (seconds) with R=70 with CCD detector					d (pc)	Counts from planet (s ⁻¹) in line	Planet counts in continuum (avg)	Q from dif-fraction	Q from scattering
2267	2304	2378	2603	2979					
7189	7479	8061	9822	12784	5	0.0228	0.0485	10	1
59350	66176	79869	121113	190045	10	0.0048	0.0101	3	1
441967	522169	682707	1164727	1968453	15	0.0014	0.0030	2	1

Figure 2.6-7 Classical Coronagraph Spectral Performance Table (2)

2.6.2.2 Spectroscopic Performance Summary

Spectroscopic detection of H₂O and O₂ at terrestrial levels in an Earth mass planet is possible with both the SP coronagraph and CL coronagraph designs, for distances up through 10 pc. At 15 pc, detection is precluded by either our Inner Working Distance (SP coronagraph) or excessive integration times (CL coronagraph). At a distance of 10 pc, we can detect H₂O with integration times <15 hours, even for the case of a ? 10 exozodi level. The corresponding integration times at 10 pc for O₂ are less than two days in most cases.

2.6.3 Survey of Nearby Stars for Terrestrial Planets

Either architecture will allow a search of 150 stars for Earth-like planets in less than two months. Of the 259 stars in the TPF reference list, 205 can be searched for an Earth analog in a reasonable (<40 hr per star) integration time with the SP coronagraph design, and 252 can be searched in <40 hr integration time per star with the CL coronagraph. The time to search the 150 most favorable stars (once each) is 50 days with the SP coronagraph and 15 days with the CL coronagraph.

The difference in integration time is primarily due to the much narrower azimuth range of heavy starlight suppression with the SP coronagraph, at angles <100 milliarcseconds from the target star. Our calculations used a dual-pupil mask, which is what we presented at the FAR. As stated earlier, the use of higher numbers of shaped pupils in the mask will widen the usable azimuth range, but the required numerical simulations have not yet been done. Therefore, the actual performance for the SP architecture will be closer to that of the CL coronagraph than indicated by the tables below.

We accounted for the ecliptic latitude in our calculations of the noise contribution from local zodiacal dust (pathlength proportional to 1 / sin[ecliptic latitude], an increase towards the ecliptic at least as steep as the observed dependence). Therefore, stars lying very close to the ecliptic require very long integration times.

2.6.3.1 Stars Where Planets Were Not Detectable

With the SP coronagraph, we excluded all stars for which the angular separation between the star and the planet was less than 50 mas. This is the Inner Working Distance for the SP coronagraph at 500 nm wavelength. The Inner Working Distance for the CL Coronagraph is smaller than any of the angular separations studied here, although the throughput decreases at smaller separations.

With the CL coronagraph, the light leakage does not fall off as quickly at large angular separations as for the SP coronagraph. There were a small number of hot stars for which $Q_{\text{diffract}} < 1$. We excluded those stars.

2.6.4 Summary of Results

Figure 2.6-8 gives the total observing time (with setup and slews) for the 50, 100, 150, or 200 stars that require the *shortest* total time to achieve SNR=5 detection of an Earth analog. This represents the most favorable case (but a realistic one, since the parameters which determine the total integration time are known in advance, and we can select the most favorable stars for our observing program). The factor of 2-3 advantage in integration time of the CL coronagraph is due primarily to its larger azimuth range for starlight suppression, so that fewer telescope repointing are needed per star. As stated above (2.6.3), use of a higher number of shaped pupils will improve the performance of the SP coronagraph.

Number of stars	Total Observing Time (d) w/ SP Coronagraph	Total Observing Time (d) w/ CL Coronagraph
50	7	3.5
100	22	9
150	50	15
200	105	25

Figure 2.6-8 Total Time for Coronagraph Design Options to Observe Each System Once

Because we can observe the most favorable potential planetary systems more quickly than the others, the graphs of cumulative observing time rise more quickly as we continue to add in stars to be observed, as shown in Figures 2.6-9 and 2.6-10. Yet we can see that a survey phase of six months still lets us observe 150 stars 12 times each with the CL coronagraph!

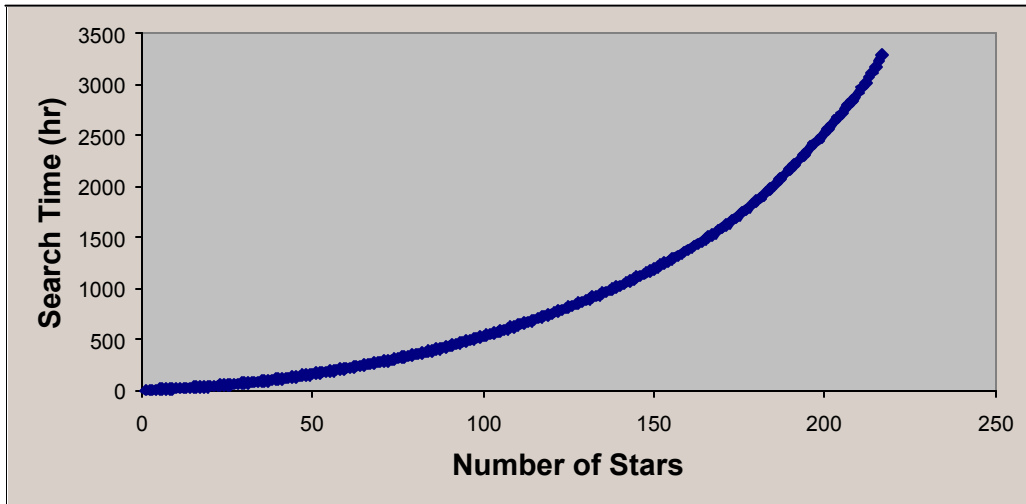


Figure 2.6-9 Cumulative Search Time for SP Coronagraph

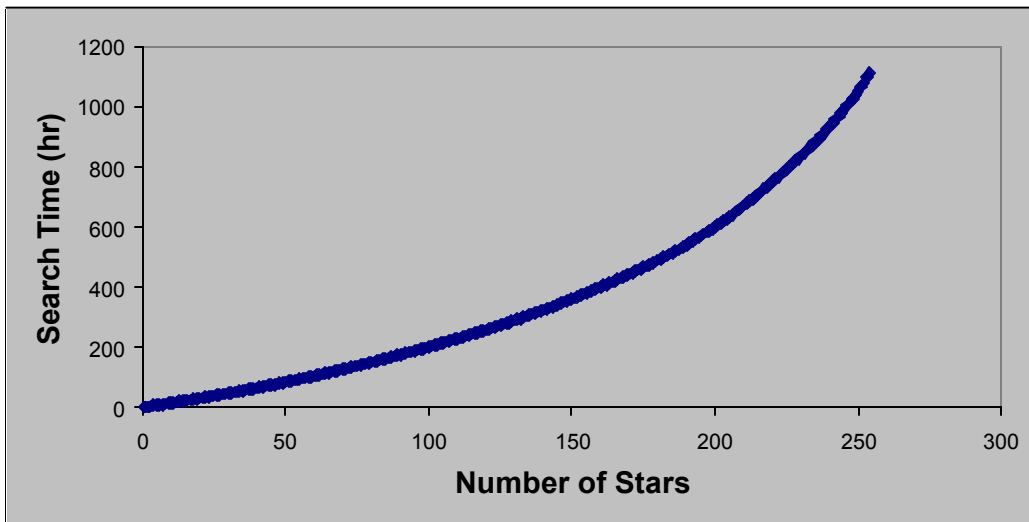


Figure 2.6-10 Cumulative Search Time for SP Coronagraph

3 Astrophysics Capabilities

The particular advantages for astrophysics of our TPF single-large-aperture telescope concept include its wide field and suitability for use with large detector arrays, its very highly-corrected optical wavefront (at visible wavelengths, and even in the UV), and its ability to incorporate a variety of instruments sharing the field of view either spatially or temporally. Likely instruments present, and their roles in astrophysics, will be the following:

- 1) The planet-finding coronagraph, a narrow-field, high-contrast instrument with a variety of pupil stops and image stops to achieve desired contrast rejection levels in specified spectral bands at selected angular separations from bright sources. Adding spectroscopic components to determine distributions of material species and velocities, it will be particularly effective in studying black-hole dynamical environments close to the central region.

2) A wide-field UV/visible imager can be used simultaneously with the narrow-field coronagraph for acquisition of deep-field surveys in directions near the coronagraphic target, or it can be used in any direction to gather very high-resolution images of faint objects, such as distant galaxies. This will be more effective over wide fields than is possible with ground-based telescopes using adaptive optics (AO), because AO correction is very difficult over large fields, and also because of the opacity and/or brightness of Earth's atmosphere in many wavelength regions. TPF's space-based performance not only would provide 10 milliarcsecond imaging over a field at least 2 x 2 arcminutes, but also permits high photometric stability for detection of transient events and secular variations. Together with its high-resolution and high-contrast performance, the imager's spectral range should enable much progress to be made in investigating stellar environments around very young stellar objects (YSOs) over a wide range of stellar properties (ages, metallicities, etc.), yielding many facts about the YSO disks and jets.

3) A powerful UV/visible spectrograph can take advantage of the telescope's large aperture, high resolution, and wide spectral coverage. With a collecting area 8 times that of the HST, the spectroscopic sensitivity can be up to 64 times better than HST. This permits studies of stellar oscillation of faint stars (using Doppler shifts and other signs of physical variations), of detailed dynamics of distant galaxies, of the formation and distribution of chemical elements (including clarifying the influence of stellar end-phases upon galactic chemical evolution, and of galaxy building (from stellar population studies in nearby galaxies).

4) Incorporation of polarizing filters in the observatory pupil plane enables measurements revealing detailed structure and constitution of the Interstellar Medium, which is, of course, the starting point for star formation.

Key unanswered questions addressable with a large-aperture UV-optical space telescope might be:

Where is the rest of the unseen universe?

What is the interplay of the dark and the luminous parts of the universe?

How old is the universe?

Where are all the baryons?"

How did the intergalactic medium collapse to form the galaxies and clusters?

When did stars and black holes form?

What are the building blocks of galaxies?

When were galaxies, clusters, and stellar populations assembled into their current form?

Are massive black holes a natural part of most galaxies?

By detecting Cepheid variable stars beyond the Coma cluster of galaxies, a visible-light TPF can measure H_0 to 1% accuracy. When combined with MAP's measurement of the distance to the surface of last scatter, this yields an accurate estimate of the universe's equation of state. Measuring surface brightness fluctuations out beyond Coma will help trace the large-scale distribution of matter.

Detailed studies of high-redshift supernovae will deepen our knowledge of these important "standard candles". With its wide-field capability, the visible-light TPF could also trace the distribution of dark matter as a function of distance, via gravitational lensing. The resulting understanding of mass power-spectrum evolution would provide one of the most sensitive astronomical probes of the natures of dark matter and dark energy.

4 Mission Feasibility

4.1 Technical Risk Areas

The major risks to the visible-light coronagraph architecture fall into two broad categories: science risks and technical risks. The science risks are those involving astrophysics, and occur even if the instrument can be made to work perfectly. If the abundance of Earth-like planets (as will be measured with the recently approved Kepler mission) is low (less than ~8% of stellar systems), a visible light coronagraph is not a viable architecture. In order to measure a useful sample of planets, the mean distance to target stars would be large, and the typical star-planet angular separation would be smaller than our IWD.

		Abundance of Earth-like Planets (e.g., Kepler)	
		Low ($< \sim 8\%$ of stars)	Medium to High ($> \sim 8\%$ of stars)
Level of exozodiacal emission around target stars (as determined by, e.g., LBT CODEX, Keck interferometer,)	Low (most are < 10 zodis)	Interferometer with large baseline and apertures	Either coronagraph or interferometer
	High (most are > 10 zodis)	Neither in the near future	Coronagraph

Figure 4.1-1 Preferred Architecture vs. Abundance and Detectability of Earth-like Planets

The primary technical risk areas for the TPF Coronagraph that require maturation before proceeding to Phase A (and the TPF Architecture downselect) are:

1. **Large optics** – We require a lightweight, high precision, monolithic $4 \text{ ? } 10$ m primary mirror. The key requirements are a density $< 25 \text{ kg/m}^2$ and surface errors $< 2.5 \text{ nm rms}$ at spatial frequencies of $3\text{-}10^4$ cycles per aperture major axis.
2. **Thermal control and structural motion** – Wavefront Distortions over a several hour observation must be 0.03 nm rms or less at critical spatial frequencies
3. **Amplitude uniformity & stability** – The goal is an intensity uniformity of $1.5 \text{ ? } 10^{-4}$, with the requirement a factor of 10 looser.
4. **Deformable mirrors** The required adjustment precision and stability over multi-hour integrations is $< 0.1 \text{ nm}$.
5. **Wavefront sensing** – must be adequate for $< 0.1 \text{ nm}$ control
6. **Large Lightweight Shields** – This includes deployable sunshields and baffles, and will be an enhanced version of those used for NGST. The technical risk areas can be largely validated in ground testing. In particular, ground demos would validate the actual performance (accuracy and stability) of deformable mirrors, wavefront sensing schemes, and the construction of stable, lightweight demonstrator mirrors of high surface quality.

Precursor missions can validate the technologies at a system level, in addition to obtaining observations that are critical for science planning. These missions would have 1.5-4 m diameter coronagraphs. They have been already proposed as MIDEX and Discovery missions, and as NRA studies. Of particular interest for detection of extrasolar terrestrial planets, a TPF coronagraphic precursor with a 4 m aperture would be able to detect "Earths" 1 AU from their parent sun-like stars at distances up to 8 pc (125 mas separation would be 4 Airy radii at $\text{?} = 0.5 \text{ ?m}$), which permits such detections for about 40 stars. If "Earths" exist near just 10% of such stars, then the 4 m precursor might detect 4 of them.

4.2 Estimated Cost

We estimate life-cycle costs for TPF using three methods. The results provide a range of estimates which agree to within twenty percent. We derive cost estimates of \$1.9B using parametric models, \$1.27B using our top-down method, and \$1.32B using our bottom-up method. We conclude that a total life-cycle cost estimate for the TPF visible-wavelength coronagraph is \$1.5B, the average of these three results. (All costs are in FY2002 dollars).

Estimating costs for a well-defined project which uses existing technologies is difficult, as is on-schedule and on-budget performance against those estimates. Estimating costs four years in advance, for an eight-year development and five-year on-orbit mission which comprises significant technology development is correspondingly more difficult. Thus, we believe it's critical to understand and detail the assumptions, complexities, risks, and other inputs, and also to use multiple tools and techniques to best probe and understand the cost estimates.

In each of our cost estimating techniques, we include Pre-Phase A (Technology Development), Phases A and B (Formulation), and Phases C/D and E (Implementation, consisting of Design, Build, Test, Launch, Deployment, & Mission Operations). Using current best estimates, we include \$470M to account for technology development (\$50M), launch, (\$220), and mission operations and operations facilities (\$200M). We don't include cost reserves in any of the estimates.

For each technique, we use the same set of conservative assumptions, including:

- ?? TPF will be a long-life (5-year requirement, with ideally a 10-year lifetime), high-reliability (low-risk) mission.
- ?? We work according to the nominal TPF schedule (presented in the following section).
- ?? Optics development will be complex.
- ?? The suite of science instruments is highly complex.
- ?? We employ low-risk management techniques throughout (e.g., a low-risk sparing philosophy.)
- ?? We don't realize cost savings from technology flow-downs from other projects.

We also recognize key uncertainties in our assumptions, including:

- ?? Development of final performance requirements.
- ?? Eventual results from ongoing modeling and design work.
- ?? Progress in key technology developments.
- ?? Definition of the science instruments and the astrophysics mission.

Because of these conservative, low-risk assumptions, we believe the range of estimates is reasonable. We also believe cost risks are relatively minor because of our current depth of detail in mission definition, considerable similarity to heritage programs, strong technology inheritance in many areas, simple readiness tests, and clear technology development roadmaps. The single-component telescope system has only a moderate number of parts and subsystems, a straightforward integration and test approach, and relatively low system risk.

Our *parametric estimate* **\$1.9 B**, brackets the expected cost of TPF based on comparisons to actual systems (See Figure 4.2-1). We compare mass, including the impact of aperture, which scales linearly to cost), orbit, performance (e.g., pointing accuracy), and complexity (e.g., the number of instruments, serviceability, and lifetime).

Comparison Mission	Comparison Factors					TPF Cost Estimate
	Similarity Weighting	Mass	Orbit	Performance	Complexity	
HST	4	2.0	1.1	0.9	1.4	\$1.1B
Terra	2	0.9	0.9	0.7	1.2	\$1.7B
Chandra	2	0.8	1.0	0.9	1.0	\$1.7B
QuickBird	1	(based upon proprietary data)				\$1.4B
Weighted Average TPF Cost (with added technology development, launch, and mission operations costs)						\$1.9B

Figure 4.2-1 Parametric cost estimate results for TPF

Our *top-down estimate*, **\$1.27 B**, is based on expert engineering judgement, similarity to other programs, historical information, and identification of special hardware needs and cost risks (See Figure 4.2-2). Beginning with NGST as a baseline, we polled experts on the technical and costing efforts. We accounted for differences in technical approaches, including the instrument suite, Primary Mirror fabrication and polishing, Deformable Mirror technologies, and environmental tests.

Finally, our *bottom-up estimate*, **\$1.32 B**, uses an industry-standard model modified and calibrated to our business methods. (See Figure 4.2-2). This technique, the most detailed of the three, considers the project schedule and a complete, detailed WBS, in conjunction with special attention to critical technology items. The model has been recently updated and validated against our latest actual mission costs.

WBS	Element	Top-Down Cost Estimate	Bottom-Up Cost Estimate
1.0	Technology Development	\$ 50M	\$ 50M
2.0	Preliminary Analysis (Phase A)	30	30
3.0	Instrumentation	510	550
3.1	Instrument Suite	325	
3.2	Backplane	35	
3.3	Primary Mirror	120	
3.4	Deformable Mirror	30	
4.0	Spacecraft	145	160
4.1	Bus	120	
4.2	Sunshade/Baffle	25	
5.0	Integration & Test	120	110
6.0	Launch Services	220	220
7.0	Mission Operations/Data Analysis	200	200
Total TPF Project Cost Estimate		1.27 B	1.32 B

Figure 4.2-2 Our Top-Down and Bottom-Up estimates produce similar results.

The Top-Down estimate provides a high-level comparison by hardware elements, while the Bottom-Up is the most detailed analysis of mission costs.

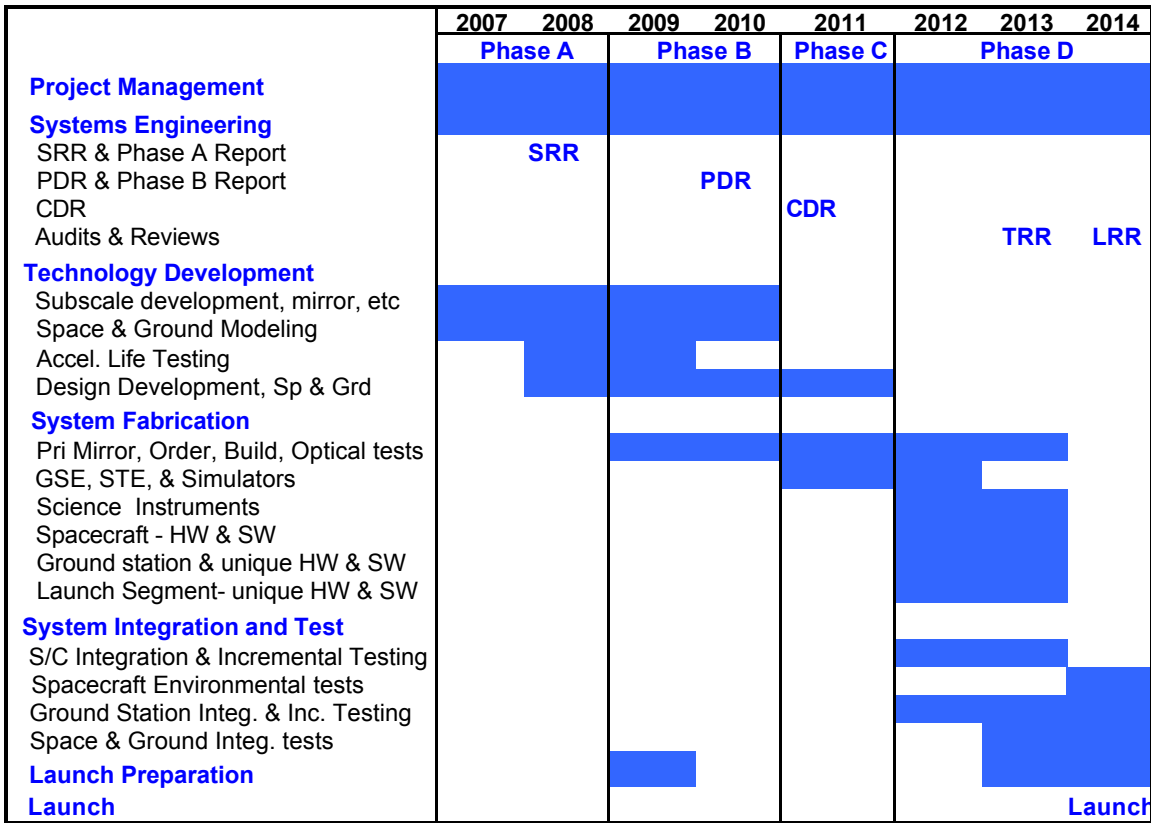


Figure 4.3-1. Our detailed schedule matches the nominal TPF schedule, identifies key tasks and milestones, and long lead-time procurements.

4.3 Estimated Schedule

We've based our schedule on the nominal TPF schedule which features a technology downselection in 2006, Phase A studies lasting to 2008, Phase B until 2010, Phases C/D culminating in launch in 2014, and operations until 2019. We've used those milestones to develop a detailed schedule (see Figure 4.3-1), paying special attention to long lead-time items and identification of technical risk areas. We believe the nominal schedule is readily accomplished and we've based our cost estimates on this schedule. Time-phased costs for the program, tied to this schedule, are shown in Figure 4.3-2.

During Phase A, systems engineering analysis activities are critical as they complete our understanding of requirements, and their flowdown to all system elements, culminating in an SRR. Technology Development explores feasibility by computer modeling, selected sub-scale developments, and life-testing of moving parts. A very long lead time is associated with the mirror, so its procurement must start immediately at the contract award. At contract award, arrangements and initial scheduling for launch also must be started. Phase B will continue this work with a heavy emphasis on specific designs leading to PDR, and preliminary development of key systems engineering documents. According to the nominal schedule, Phase C precedes the CDR. This is a time of intense design activity as well as the formulation of a detailed verification plan. However, build of test support equipment must start early for it to be ready in time. Phase D must begin with near-immediate fabrication, as little time is left between the CDR and the launch. After CDR, we begin fabrication and incremental test of each subsystem. The TRR reviews all test data to show that the system is ready for environmental test, and the LRR assesses its readiness for launch.

Despite some aggressive elements in the schedule, we believe the program can be accelerated by dedication of additional resources during the Pre-Phase A period, leading to a quicker Technology Review and selection of the final architecture class, while maintaining the low-risk implementation by identifying and mitigating technology risks beginning in Phase A.

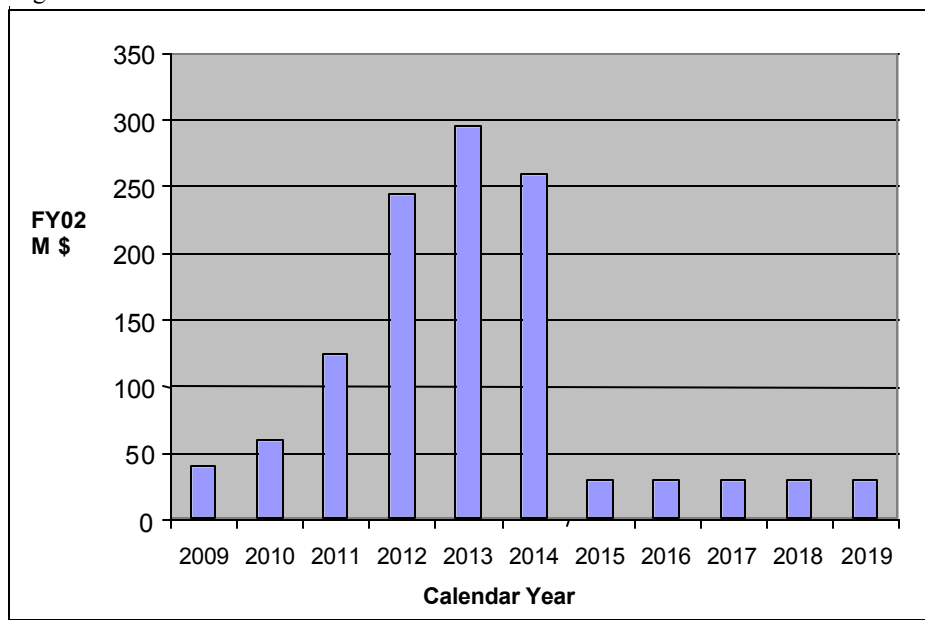


Figure 4.3-2. Our cost estimate is time-phased to show TPF's yearly development costs. For clarity, Pre-Phase A and Phase E are not shown.

REFERENCES

- N. J. Kasdin, D. N. Spergel, and M. G. Littman, "An Optimal Shaped Pupil Coronagraph for High Contrast Imaging, Planet Finding, and Spectroscopy," 2002 (submitted)
- M. J. Kuchner and W. A. Traub, "A Coronagraph with a Band-Limited Mask for Finding Terrestrial Planets," The Astrophysical Journal, May 2002 (in press)